



This is a repository copy of *Synthesis and microstructural evolution in ternary metalloceramic Ti₃SiC₂ consolidated via the Maxthal 312 powder route.*

White Rose Research Online URL for this paper:
<http://eprints.whiterose.ac.uk/158523/>

Version: Accepted Version

Article:

Magnus, C., Galvin, T., Ma, L. et al. (2 more authors) (2020) Synthesis and microstructural evolution in ternary metalloceramic Ti₃SiC₂ consolidated via the Maxthal 312 powder route. *Ceramics International*. ISSN 0272-8842

<https://doi.org/10.1016/j.ceramint.2020.03.078>

Article available under the terms of the CC-BY-NC-ND licence
(<https://creativecommons.org/licenses/by-nc-nd/4.0/>).

Reuse

This article is distributed under the terms of the Creative Commons Attribution-NonCommercial-NoDerivs (CC BY-NC-ND) licence. This licence only allows you to download this work and share it with others as long as you credit the authors, but you can't change the article in any way or use it commercially. More information and the full terms of the licence here: <https://creativecommons.org/licenses/>

Takedown

If you consider content in White Rose Research Online to be in breach of UK law, please notify us by emailing eprints@whiterose.ac.uk including the URL of the record and the reason for the withdrawal request.



eprints@whiterose.ac.uk
<https://eprints.whiterose.ac.uk/>

Synthesis and microstructural evolution of ternary metalloceramic Ti_3SiC_2 via the Maxthal 312 powder route

Carl Magnus^{1*}, Tom Galvin², Le Ma¹, Ali Mostaed³, W. Mark Rainforth¹

¹Department of Materials Science and Engineering, The University of Sheffield, Mappin Street, Sheffield S1 3JD, UK

²M&I Materials Ltd. Hibernia Way, Trafford Park, Manchester, M32 0ZD, UK

³Department of Materials, University of Oxford, 16 Parks Road, Oxford OX1 3PH, UK

Abstract

Bulk specimen containing Ti_3SiC_2 , TiSi_2 and TiC was prepared through an in situ spark plasma sintering/solid-liquid reaction powder metallurgy method using the Maxthal 312 (nominally- Ti_3SiC_2) powder as starting material. The reaction mechanism, phase constituents and evolution of microstructure were systematically investigated by X-ray diffraction (XRD), optical microscopy, scanning electron microscopy (SEM) equipped with energy dispersive spectroscopy (EDS) system, transmission electron microscopy (TEM), Raman spectroscopy, differential scanning calorimetry (DSC) and Vickers microhardness testing. Phase analysis and microstructural characterization revealed that the bulk sample contained binary ancillary phases possibly due to incomplete reaction and/or Si evaporation. The deformed microstructure around the indents revealed evidence of plasticity, intrinsic lubricity and toughening. The Microstructural and orientation relationships between the phases contained in the bulk sample are reported.

Keywords: Ti_3SiC_2 ; metalloceramic; spark plasma sintering; reaction mechanism; microstructure

1. Introduction

Upon the discovery that the ternary metalloceramic compounds with $\text{M}_{n+1}\text{AX}_n$ (MAX) chemistry (where $n = 1 - 5$, M is an early transition metal, A is an A-group and X is C or N) possess and unusual, and sometimes unique set of properties, they have been extensively

studied [1-3]. The fact that the 2-D materials known as MXenes, which cannot be synthesized directly due to their thermodynamic metastability [4-6] can be synthesized directly from 3-D MAX phases by taking advantage of the significant difference in strength between the metallic M–A bonding and covalent M–X bonding, which aids in selectively etching out the A-layer to form two-dimensional MXenes have further attracted extensive interest in MAX phases [7]. Well over 100 MAX phases have now been successfully synthesised, and in some cases ‘hybrid’ MAX phases, consisting of a partial substitution of the M or A elements have also been found to be stable [1-3, 8].

MAX phases typically exhibit properties between those of metals and conventional ceramics [1]. They have high electrical and thermal conductivity while also showing creep resistance, high temperature strength, and good resistance to thermal shock and oxidation [9]. They are stiff (Ti_3SiC_2 has around three times the stiffness of titanium with a comparable density [10]) and relatively soft compared to their binary carbide equivalents, so much so that MAX phases are easily machinable with common metalworking tools such as hacksaws or lathes [11]. Due to their layered structure, MAX phases are surprisingly damage tolerant; the layers slide, kink and delaminate to absorb the deformation, causing local hardening at the damage site [12-14]. Currently, MAX phases find applications as furnace tubes and high temperature burner nozzles, as well as electric furnace elements [10]. They have been proposed for use as latex glove formers [10], and, due to some favourable radiation tolerance studies [15-18] MAX phases are also being considered as a potential material for use within current and future designs of nuclear fission reactor [19, 20]. Their layered nature and self-lubricating properties make them a candidate for bearings and other sliding applications [21-24].

Titanium silicon carbide (Ti_3SiC_2) is a member of the $\text{M}_{n+1}\text{AX}_n$ layered compound belonging to the $\text{Ti}_{n+1}\text{SiC}_n$ system. It is the most stable ternary phase in Ti–Si–C ternary phase system and crystallizes in the space group of $\text{P6}_3/\text{mmc}$ [25]. However, its formation is compromised

by more stable binary phases (TiC, SiC and TiSi₂) due to its narrow formation region in the Ti–Si–C phase diagram [25]. The bonding in Ti₃SiC₂ is anisotropic as well as metallic-covalent-ionic in nature [26]. This unusual bonding characteristics and special crystal structure render MAX phases with unique and sometimes unusual properties [27]. Ti₃SiC₂, just like other members of the MAX phases does not melt but instead decomposes into its respective binary phases via the dissociation of Si at specific temperature in various atmosphere [28]. It is reported to be stable under vacuum or argon atmosphere up to 1600 °C [29]. All these exciting properties make MAX phases a promising next generation material suitable in a range of structural applications as a monolithic phase and/or composite [30]. Some authors have reported that the composite form, Ti₃SiC₂–TiC and Ti₃SiC₂–SiC for example, possesses superior mechanical properties than monolithic Ti₃SiC₂ [31, 32].

There are several synthesis routes to produce Ti₃SiC₂. Hot Pressing/Hot Isostatic Pressing (HIP) [33, 34], as used by Barsoum and El-Raghy in their initial paper on Ti₃SiC₂ [35], and Spark Plasma Sintering [36-39] are common methods, which produce bulk samples. Self-propagating High-temperature Synthesis (SHS) is also employed to produce a low density product, which is commonly crushed to a powder for secondary densification [40-43]. Ancillary phases such as TiC, TiSi₂ and SiC are often reported to coexist with Ti₃SiC₂ during synthesis [24, 44, 45]. However, the addition of aluminium [36, 46] in controlled amount in the starting powder mixture and/or over-stoichiometric starting powder mixture containing excess silicon [47] has been shown to reduce the ancillary phases produced.

The scope of this study is to investigate the formation of Ti₃SiC₂ via the prealloyed powder route and elucidate the reaction mechanism and the resulting microstructural evolution. Synthesizing high purity Ti₃SiC₂ is not the aim of this work but instead we seek to further contribute to the metallurgy of Ti₃SiC₂. Spark plasma sintering (SPS) is a synthesis and densification sintering process with the advantage of rapid heating rate and short sintering

time. Importantly, the short sintering time is advantageous in suppressing grain growth [48] and the range of controllability of sintering parameters enables tailoring of the evolved microstructure.

2. Material and Methods

Pre-reacted commercially available Ti_3SiC_2 powder (Maxthal 312 (nominally- Ti_3SiC_2 ; particle size 2 μm , Kanthal AB, Sweden) was used as starting powder. The composition of the as-received Maxthal 312 powder were 92 wt.% Ti_3SiC_2 and 8 wt.% TiC , respectively. The powder was initially cold-pressed in a graphite die ($\text{Ø} = 20 \text{ mm}$) in between two graphite punches with the inner wall of the die and surface of the punch covered with graphite paper to isolate the powder from the die and punches. The die-powder-punch assembly was then wrapped with graphite felt to minimize possible heat dissipation during the synthesis and subsequently loaded into the SPS furnace unit (HP D 25; FCT Systeme GmbH, Rauenstein, Germany) as shown in Fig. 1. The consolidation was carried out at a sintering temperature 1400 °C with a hold time of 5 min. The heating rate was 100 °C/min whilst the load (54 MPa) was applied at room temperature and removed at the end of the dwell time. During the synthesis, the chamber was maintained under vacuum (10^{-2} Pa) and the temperature was controlled by a thermocouple that measured the temperature in the interior of the graphite punch. The sintering temperature was selected based on a preliminary test which ensures the bulk composition falls within a three-phase region as purity of the bulk sample is not the scope of this work.

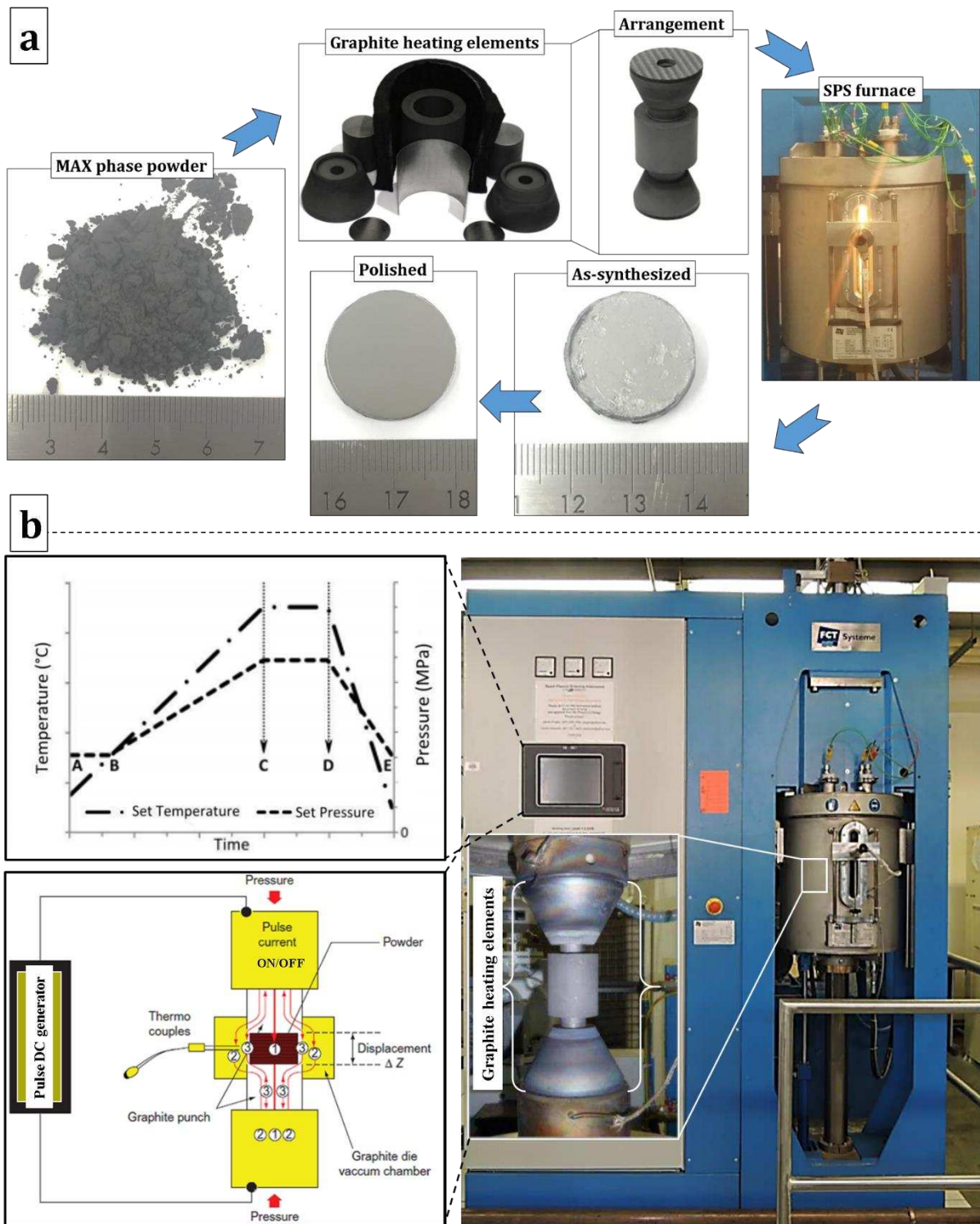


Fig. 1. (a) punch-powder- die assembly and (b) SPS furnace unit and associated sintering parameters.

2.1. Characterization

X-ray diffraction (XRD) patterns were obtained with a $\theta - 2\theta$ diffractometer (Bruker D2 Phaser, Germany) using Cu $K\alpha$ radiation source in steps of 0.02° at 1 s/step. The surface

layer of the as-sintered disc was removed by grinding prior to XRD analysis. Phase identification was performed using DIFFRAC EVA software suite whilst the phase quantification was obtained by Rietveld refinement (TOPAS) from the diffraction pattern collected in the 5–80° (2 Θ) range using X'pert³ diffractometer (Malvern Panalytical, UK). Microstructural evolution was investigated using scanning electron microscopy (SEM; Inspect F50, FEI The Netherlands) equipped with an EDS detector (Oxford Instruments X-Max/Aztec Nanoanalysis, UK) and transmission electron microscopy (TEM; Philips EM420/120 kV and JEOL JEM-F200/200 kV). TEM electron transparent samples from selected areas were prepared using a focused ion beam (FIB; FEI Helios NanoLab G3 UC, FEI company, The Netherlands). The Vickers hardness (HV) of bulk sample was measured using an indentation load of 19.6 N for 15 s (DuraScan G5 emcoTEST, Austria). The density of the bulk sample was measured following mirror-like metallographic polishing down to 0.5 μm diamond paste by the Archimedes' method in water at ambient conditions. Raman analysis was carried out ex-situ on the polished surface by employing a Si-calibrated inVia Raman spectrometer (Renishaw plc, UK) with an Ar laser ($\lambda = 514.5 \text{ nm}$, laser output power 20 mW) and a 50x objective lens (spot size of 2 μm). In order to further understand the phase transformations and reaction mechanisms during synthesis, simultaneous thermal gravimetric analysis (TGA)-differential scanning calorimetry (DSC) experiment was conducted on the Maxthal 312 powder (Q600, TA Instruments) from 25 to 1500 °C in a high purity dynamic nitrogen atmosphere using Al₂O₃ crucible.

3. Results and Discussion

3.1. Morphology of Maxthal 312 powder

The morphology of the as-received Maxthal 312 powder is shown in Figs. (2) and (3). Fig. 2 shows the characteristic lamellar nature of the Ti₃SiC₂ MAX phase compound, whilst Fig. 3

is an EDS elemental map which reveals the coexistence of TiC particle in the as-received prealloyed powder in the form of an ancillary.

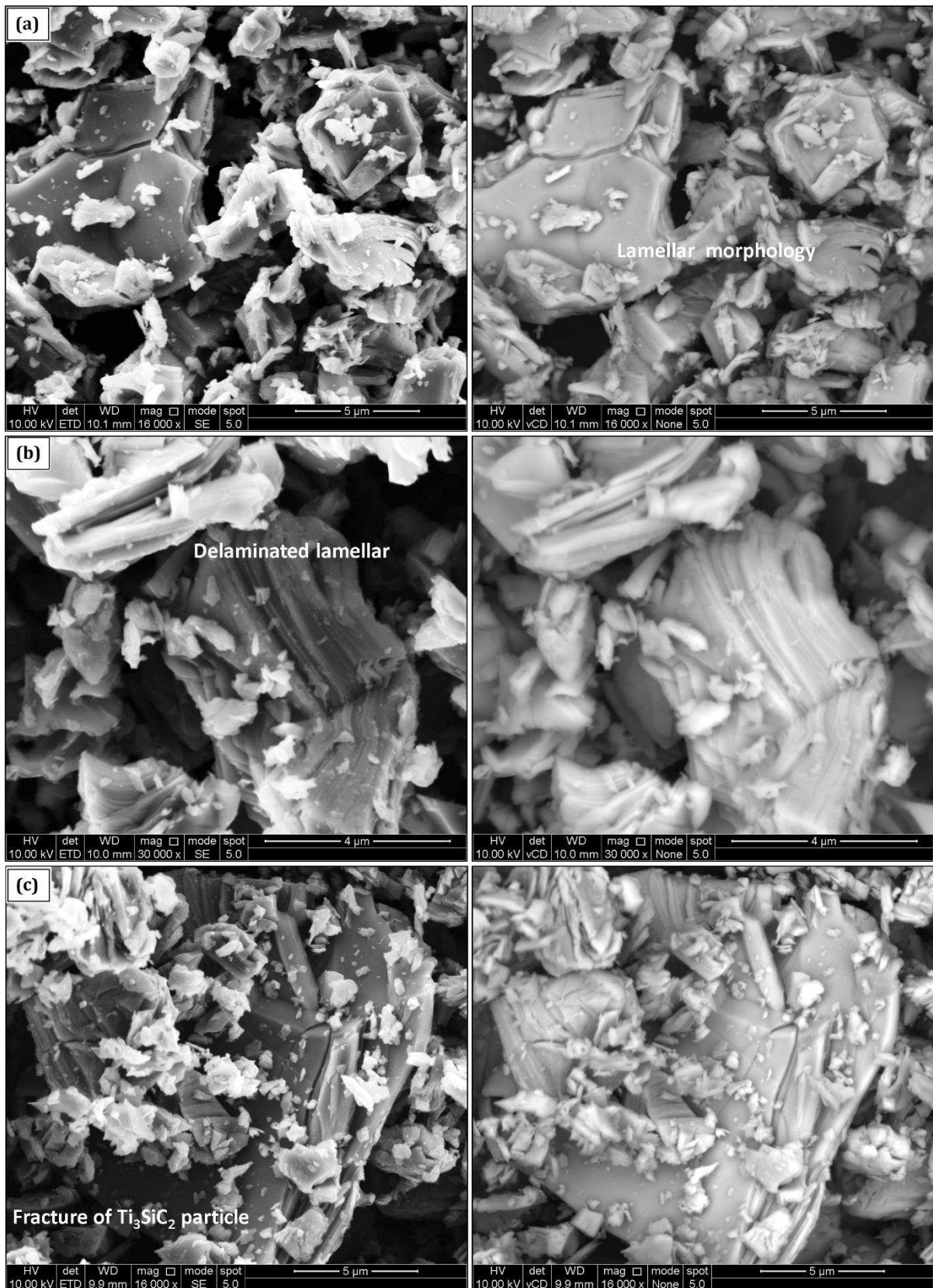


Fig. 2. SEM (SE–BSE) micrographs showing the morphology of the as-received Maxthal 312 (nominally- Ti_3SiC_2) powder.

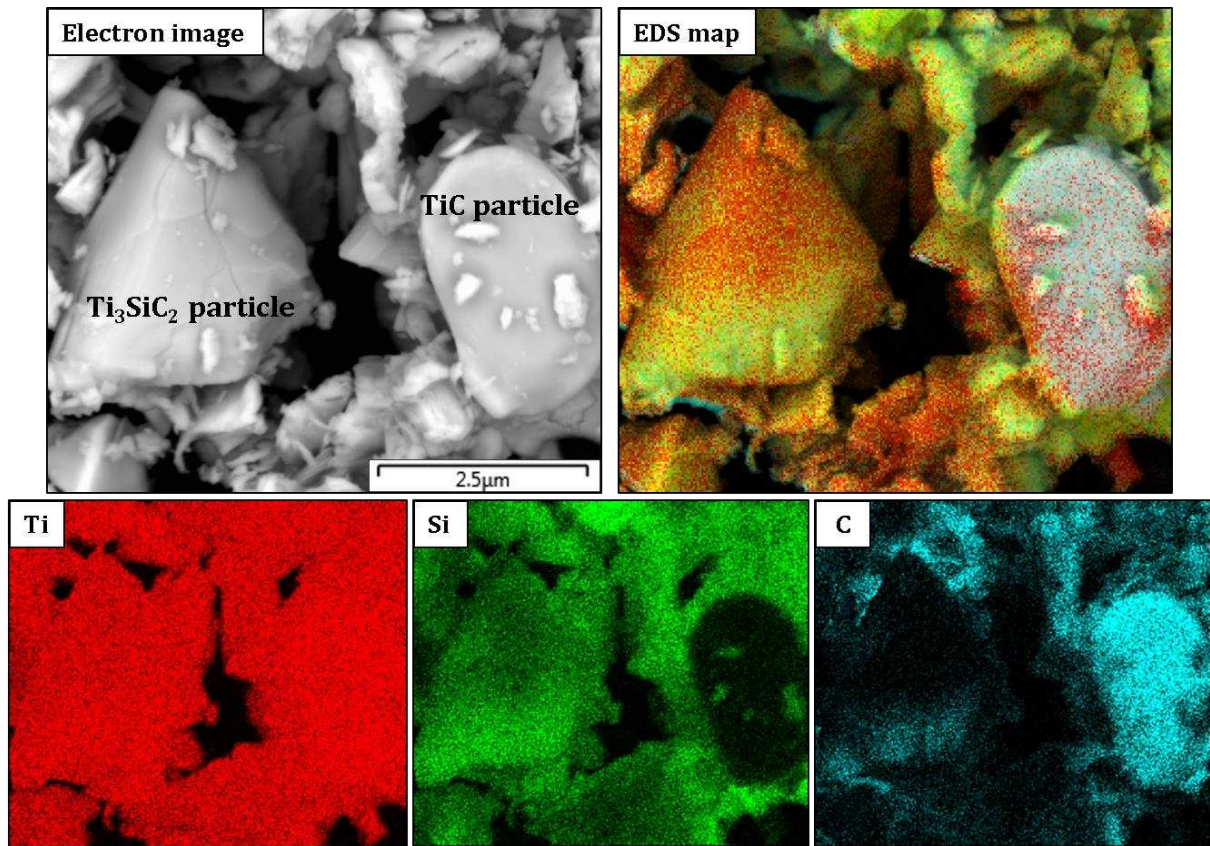


Fig. 3. EDS elemental mapping of the as-received Maxthal 312 (nominally-Ti₃SiC₂) prealloyed powder.

3.2. Phase analysis and densification

X-ray diffraction (XRD) from the as-received prealloyed Maxthal 312 powder confirmed Ti₃SiC₂ as a major phase and some minor TiC intermetallic phase is shown in Fig. 4.

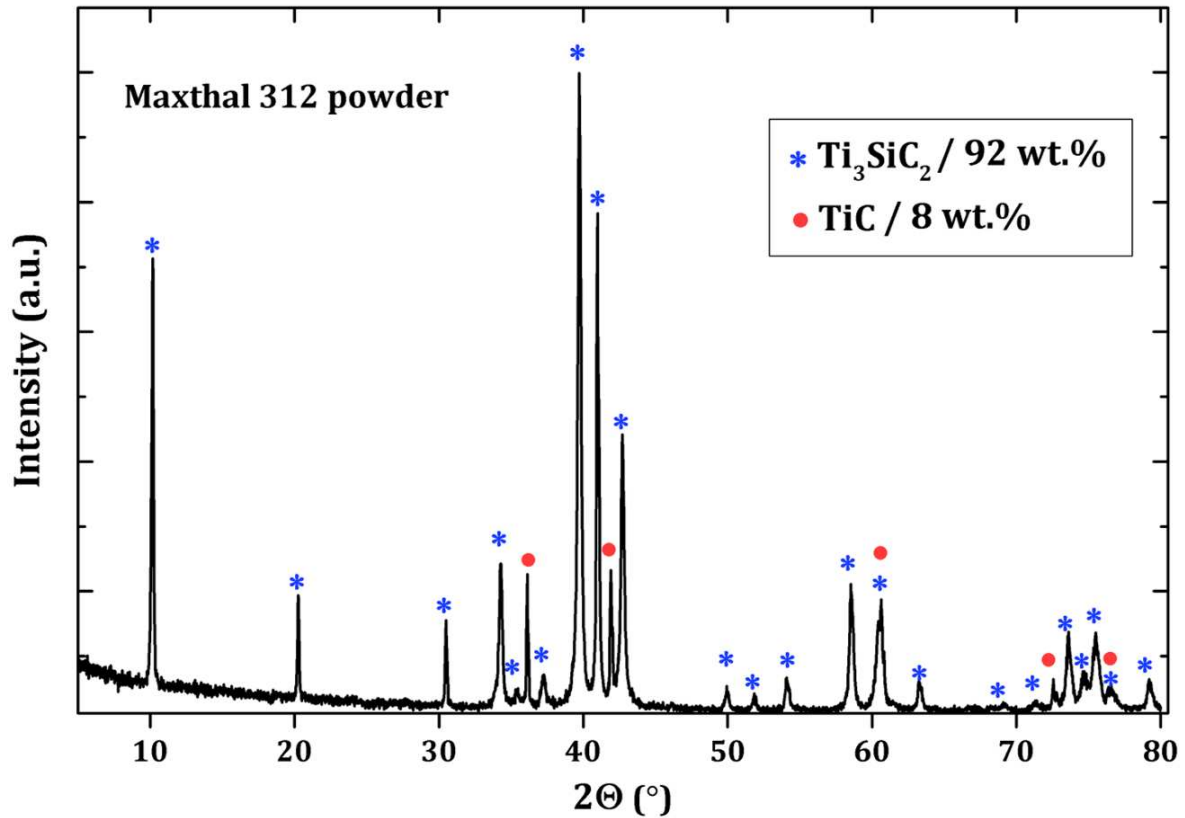


Fig. 4. XRD pattern of the as-received Maxthal 312 (nominally- Ti_3SiC_2) powder.

The XRD patterns showing the phase evolution of the bulk sample following spark plasma sintering of the prealloyed Maxthal 312 powder is given in Fig. 5. It can be seen from the diffraction pattern that the bulk sample consists of three phases: Ti_3SiC_2 , TiC and TiSi_2 , respectively. In comparison to the as-received prealloyed powder X-ray diffraction pattern, additional peaks were observed, especially two strong peaks at $2\theta = 39^\circ$ and 43.2° , which correspond to TiSi_2 peaks evolved after synthesis.

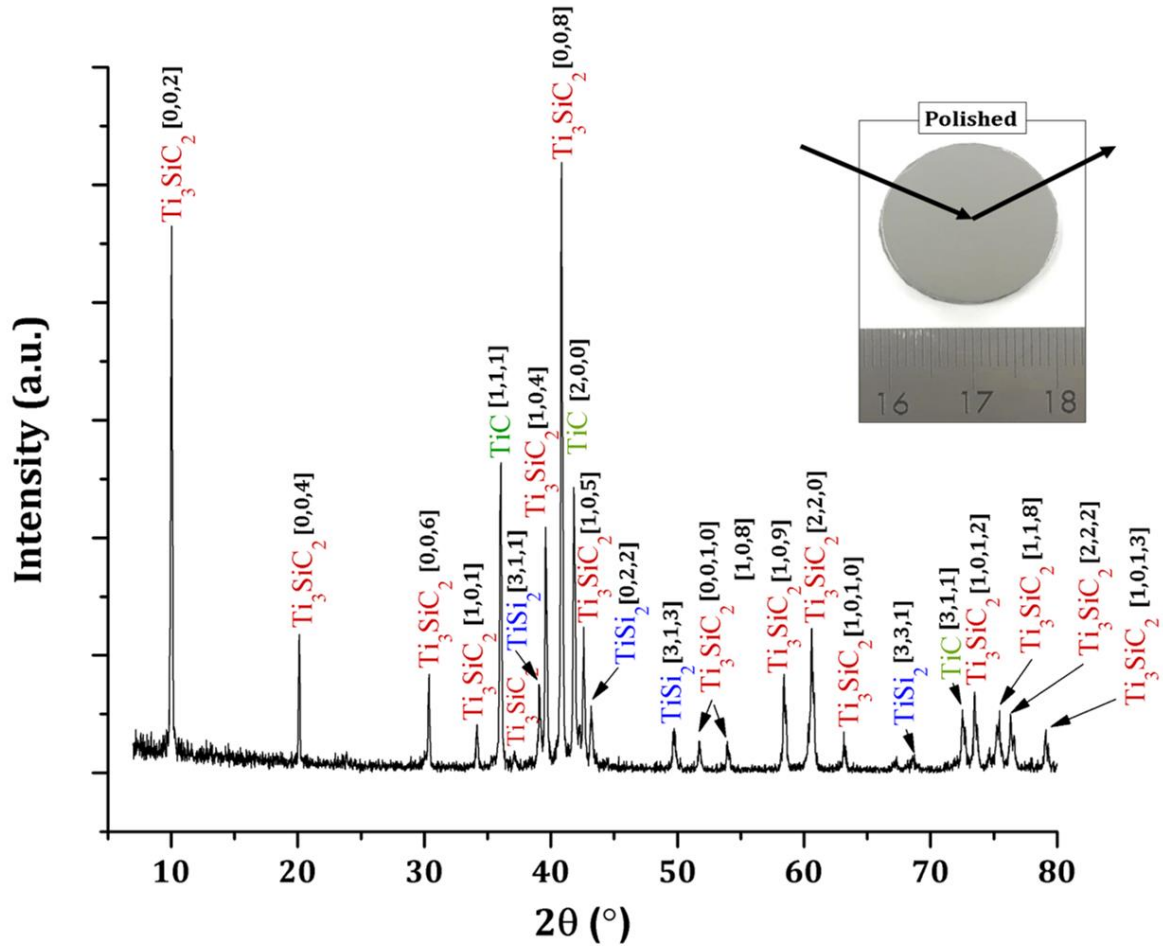


Fig. 5. XRD pattern of the synthesized sample disc after polishing. Inset shows the polished disc.

Fig. 6 shows X-ray diffraction (XRD) pattern of the bulk sample ($2\theta = 5^\circ - 80^\circ$) alongside Rietveld refinement of the pattern. The Rietveld refined parameters are $R_{wp} = 6.532$ and $\chi^2 = 3.146$, respectively. The bulk sample contained 51.8 wt.% Ti_3SiC_2 , 36.4 wt.% TiC and 11.8 wt.% $TiSi_2$, respectively. The refinement data showed strong preferred orientation in the 002 direction. This is in agreement with our earlier work which indicated preferred orientation of Ti_3SiC_2 along the pressing direction during the SPS synthesis [24]. The relative density of the polished disc was 99 % upon taking into account the phase fraction of the constituent phases and their corresponding theoretical densities, respectively.

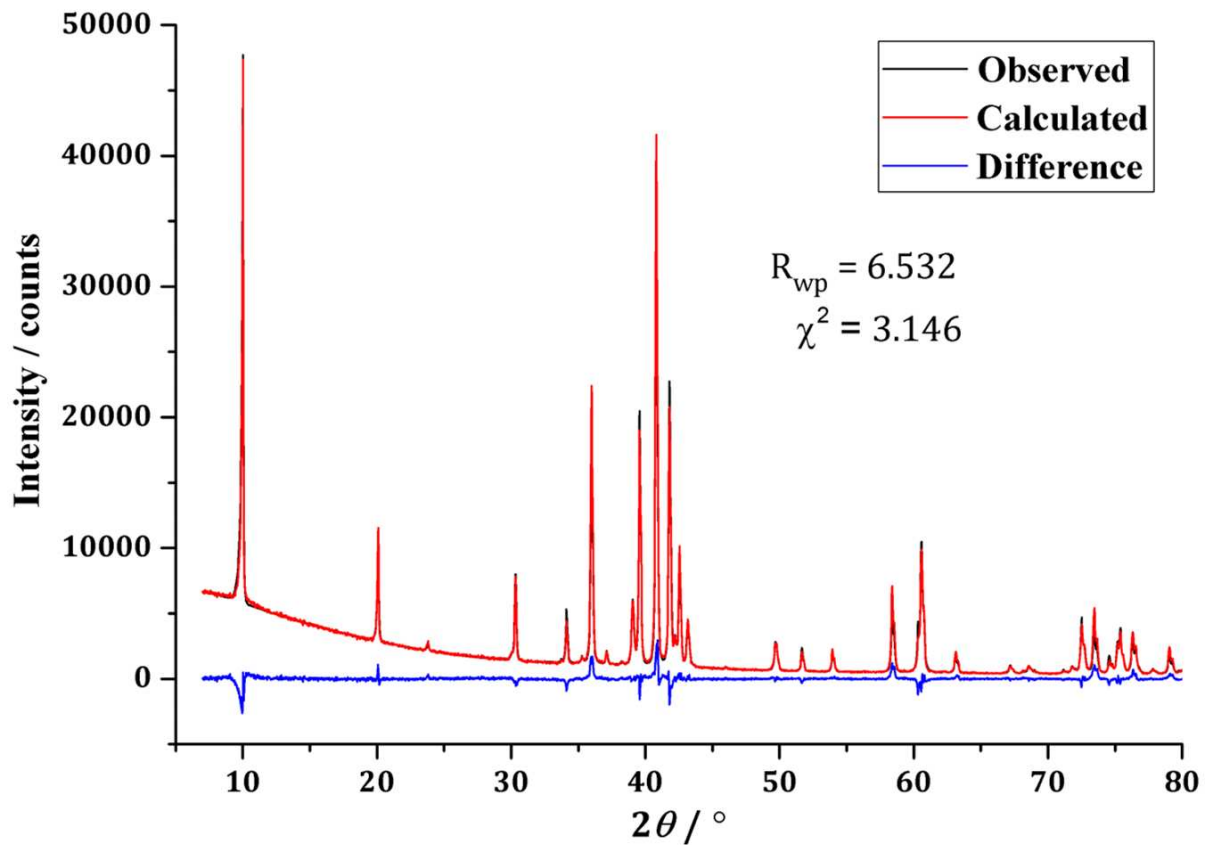


Fig. 6. Rietveld refinement of the XRD pattern of the Bulk sample in 2θ range from 5 to 80° .

3.3. Microstructural evolution and EDS analysis

SEM backscattered electron (BSE) micrographs of the polished unetched bulk sample is shown in Fig. 7. According to the EDS analysis (Fig. 8) the bright phase is the Ti_3SiC_2 phase whilst the dark contrast is the TiC phase. Those with the medium contrast are the TiSi_2 phase (white arrow in Fig. 8 map spectrum) - an intermediate eutectic liquid phase leading to the formation of Ti_3SiC_2 that has not been fully consumed [49]. According to Refs. [50, 51], the reaction mechanism leading to the formation of Ti_3SiC_2 is a solid-liquid reaction partly due to the formation of Ti–Si eutectic liquid (eutectic temperature 1332°C) and/or liquid Si formation (T_m of Si = 1414°C).

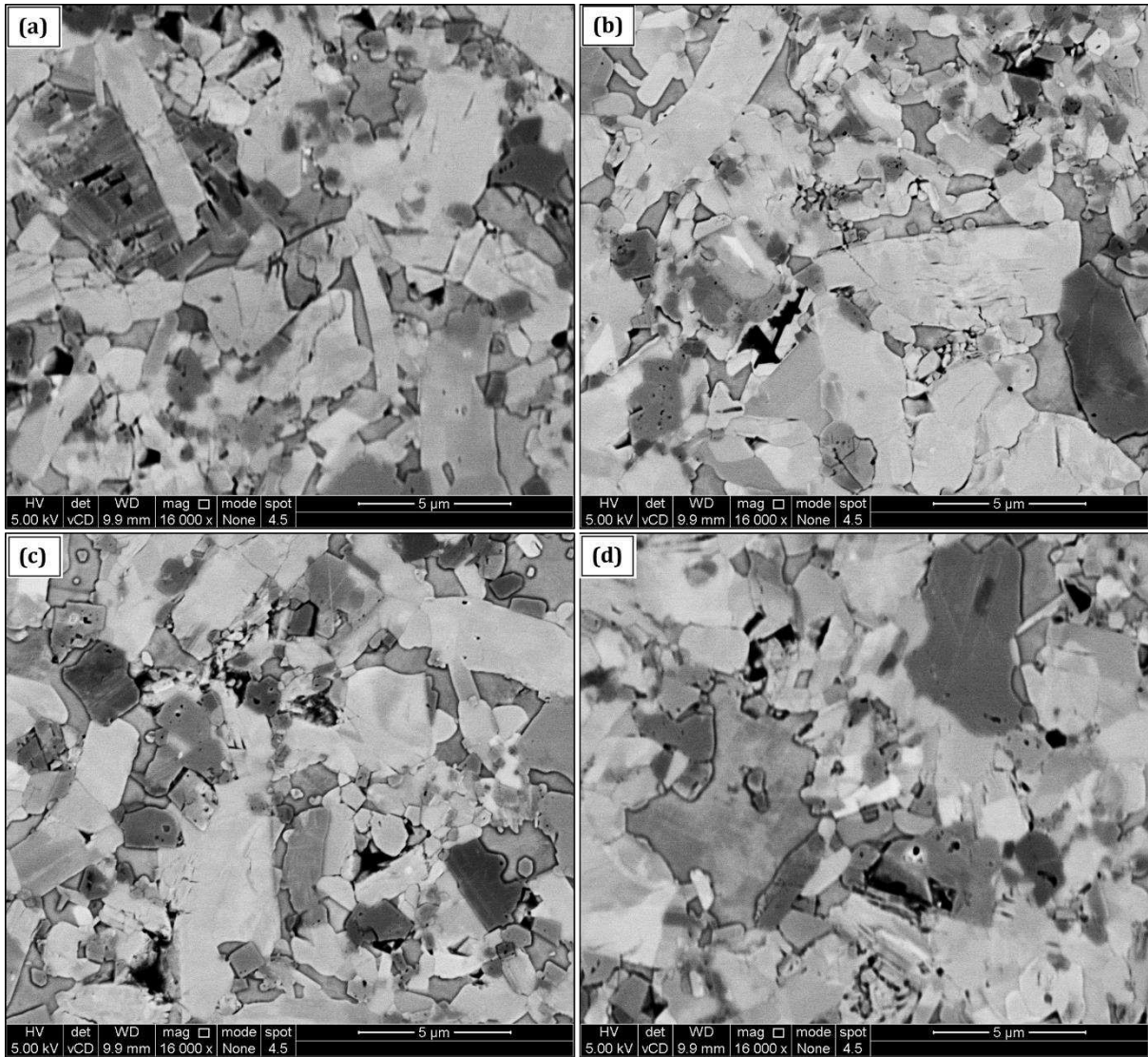


Fig. 7. Backscattered electron (BSE) images of the bulk sample produced by SPS using the Maxthal 312 powder. Note the homogenous dispersion of the in situ formed TiC in the Ti_3SiC_2 matrix.

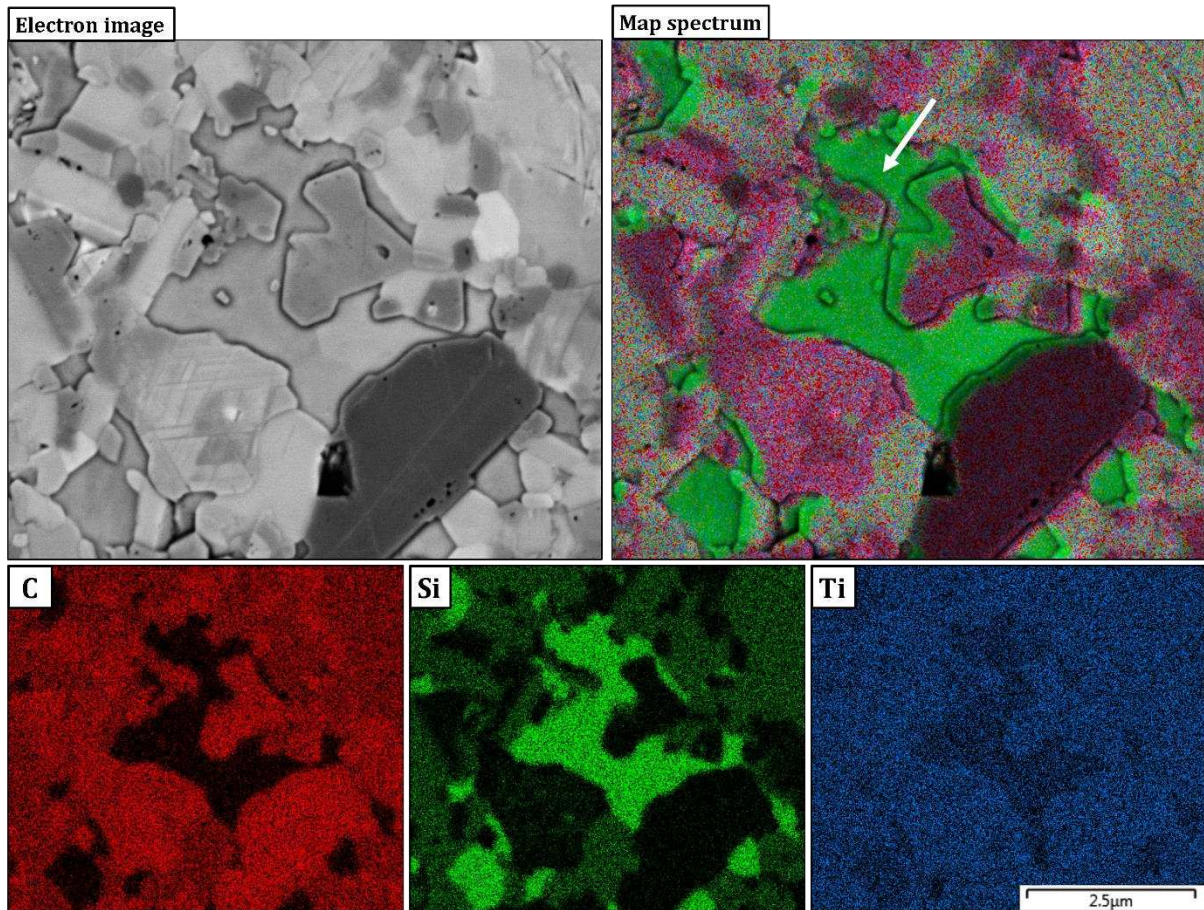


Fig. 8. Identification of particular phases in the bulk sample by EDS elemental map analysis.

Fig. 9 shows TEM images obtained from the bulk sample revealing an area containing the Ti_3SiC_2 grains. The plate-like morphology (Fig. 9(a)) typical of MAX phases can be seen alongside with evidence of basal plane dislocation (Fig. 9(b-d)) as reported elsewhere [52]. Basal plane dislocations play a key role during room-temperature deformation of MAX phases as they possess fewer than five slip systems needed for polycrystalline ductility [52, 53]. The steps along the grain boundary (red arrow in Fig. 9(b)) is an evidence of slip along the basal planes [10].

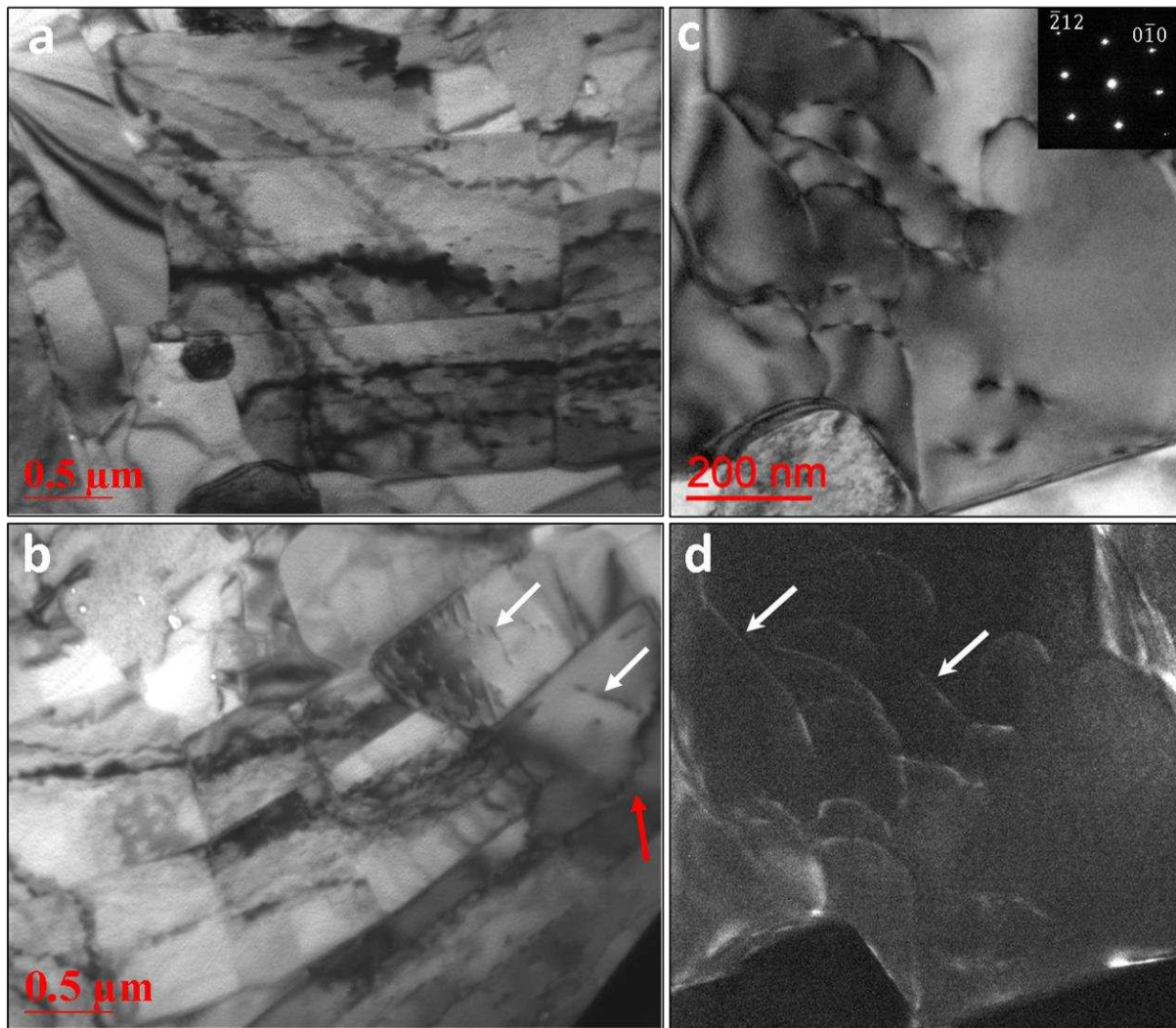


Fig. 9. (a) BF-TEM micrograph showing the plate-like morphology of the Ti_3SiC_2 grains, (b) BF-TEM micrograph showing evidence of basal plane slip (red arrow) and basal plane dislocation (white arrow), (c) BF-TEM image obtained from a Ti_3SiC_2 grain along the $[101]$ direction and (d) DF-TEM image of dislocation shown in (c) imaging with $g = \bar{2}12$ (white arrows show edge-on basal plane dislocations).

3.4. Thermal behaviour of the Maxthal 312 powder

Fig. 10 shows the simultaneous DSC/TGA thermogram recorded during the heating of the Maxthal 312 powder at $20\text{ }^\circ\text{C}/\text{min}$ from 40 to $1500\text{ }^\circ\text{C}$ in flowing Ni. Exothermic peaks (518 , 602 and $735\text{ }^\circ\text{C}$) corresponding to anatase and/or rutile TiO_2 layers were detected up to $900\text{ }^\circ\text{C}$. The observed mass increase in this temperature range is linked to the oxidation of

titanium in agreement with a previous report [54]. The DSC curve further exhibited three broad overlapped exothermic peaks (1052, 1137 and 1232 °C) as the temperature is further increased. Considering the temperature of these exothermic peaks and the SEM-EDS analysis of the phases in the bulk sample sintered to 1250 °C (Fig. 11), it can be concluded that these peaks correspond to the evolution of TiSi_2 and Ti_3SiC_2 phases. In particular the Ti–Si eutectic liquid will provide a direct route for the formation of Ti_3SiC_2 once the pre-existing TiC particles reacts with the Ti–Si liquid phase as proposed by Sato et al. [55] and Zhang et al. [56]. This conclusion is also in agreement with the thermogravimetric results obtained by Kero et al. [49, 57], as well as observations in this work revealing the growth of Ti_3SiC_2 takes place within the Ti–Si liquid phase (electron image in Fig. 11). The last exothermic peak at 1478 °C may be attributed to TiC_x formation due to Si evaporation induced Ti_3SiC_2 decomposition as the temperature exceeds the melting point of Si (1414 °C). Fig. 12 shows the XRD pattern obtained from the decomposed Maxthal 312 powder following the thermogravimetric analysis. The phases in the decomposed powder (i.e., TiC_x , TiO_2 and Si) are in good agreement with the exothermic peaks during the thermal analysis.

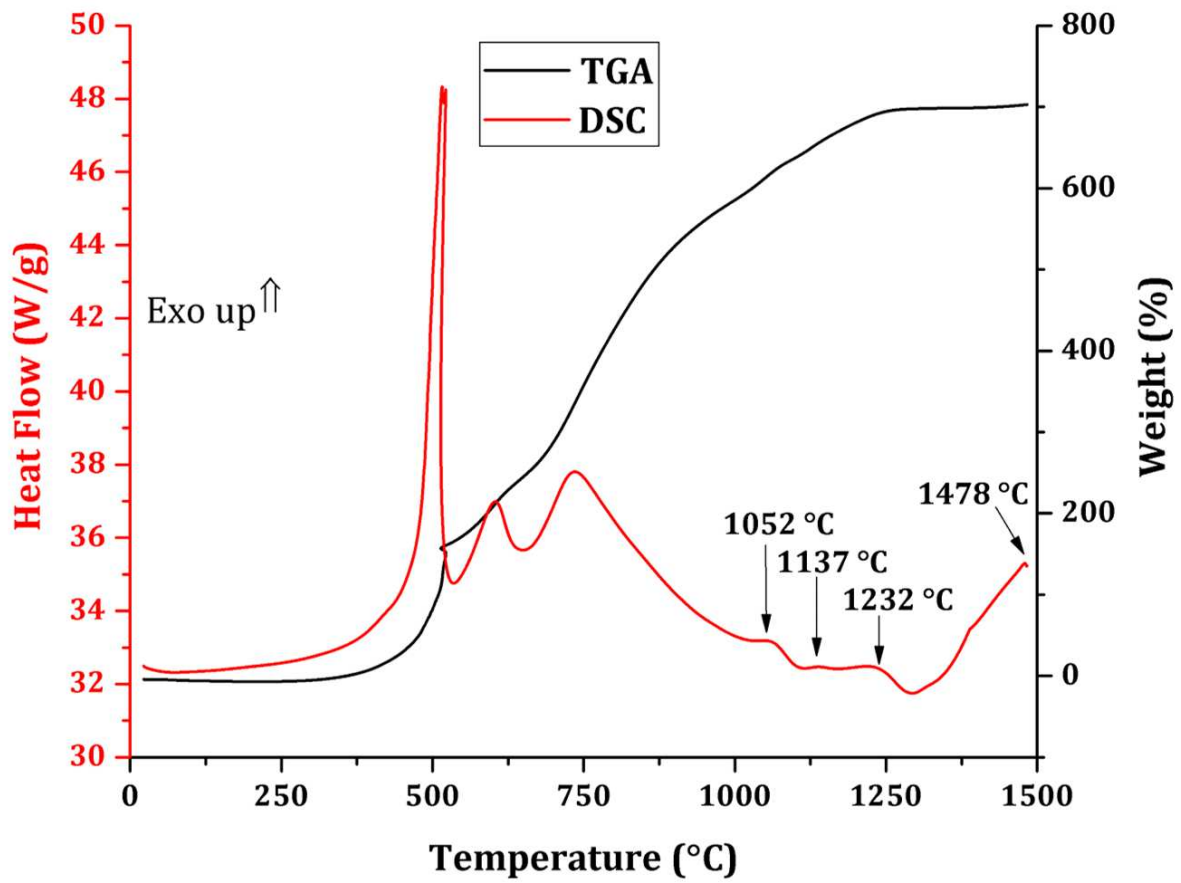


Fig. 10. TGA/DSC plot of the thermogravimetry analysis of Maxthal 312 (nominally-Ti₃SiC₂) powder.

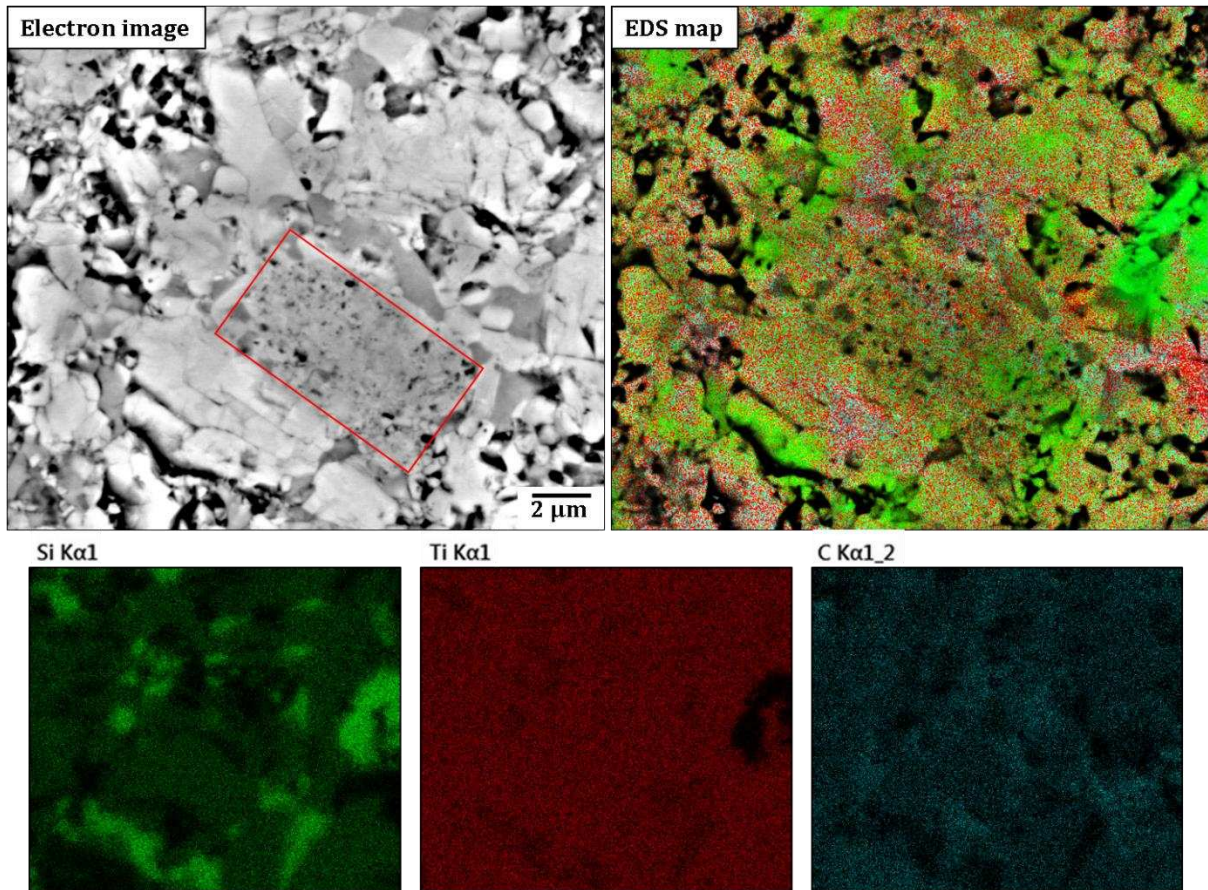


Fig. 11. EDS elemental map showing the evolution of phases in the bulk sample synthesized by SPS to 1250 °C. The highlighted section in electron image (red rectangle) shows the growth of the Ti_3SiC_2 grains.

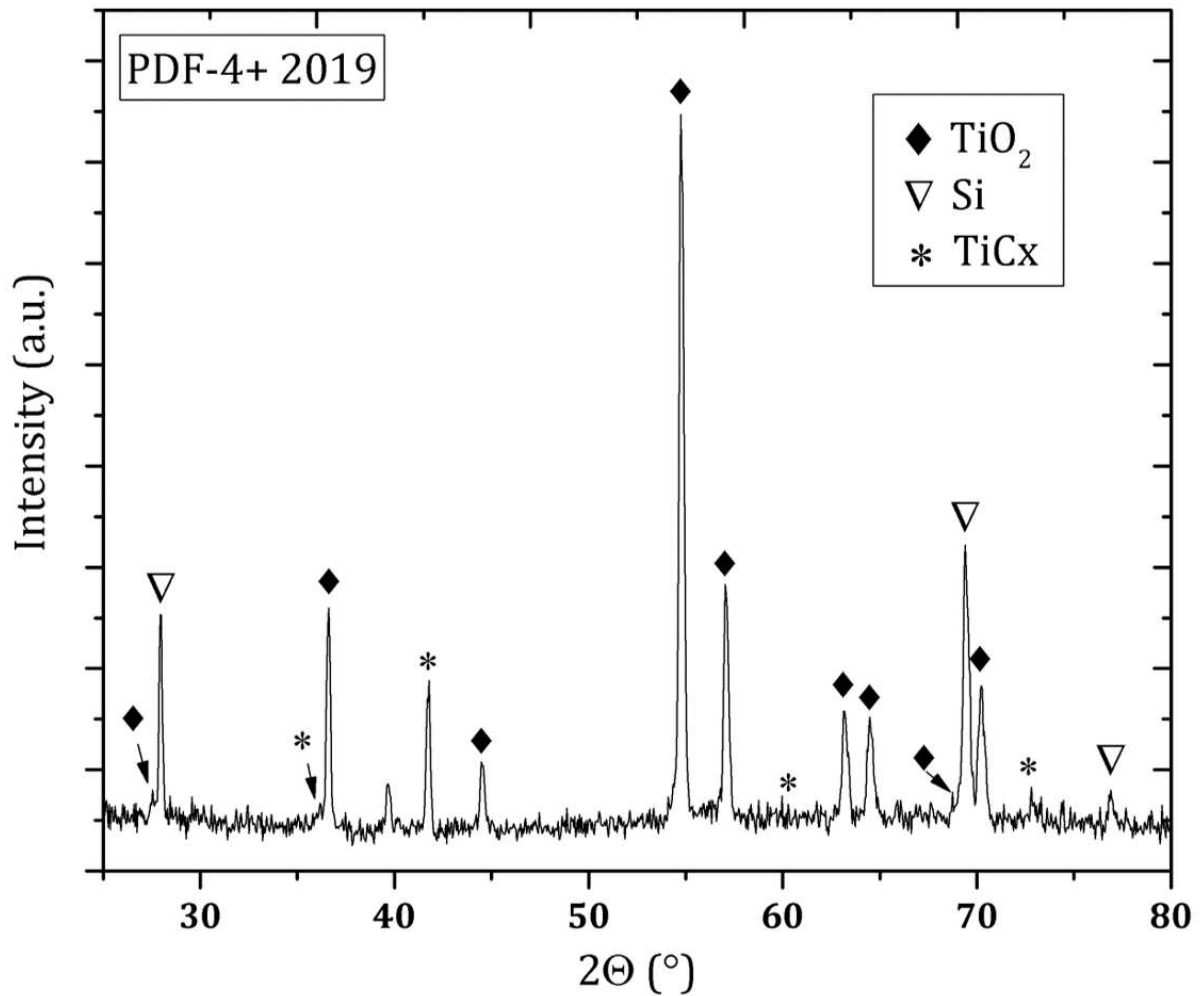
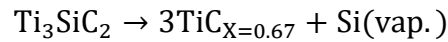


Fig. 12. X-ray (XRD) diffraction pattern of the decomposed powder after TGA/DSC thermal analysis.

3.5. Pore formation in Ti_3SiC_2

The pores formed during the synthesis of Ti_3SiC_2 such as those shown in Fig. 13 are derived from the following aspects: the original particle gap; interstitial pores left during the pressing procedure; lack of densification; generation of new phase in the sintering process; Si deintercalation linked to the high vacuum pressure during the SPS and/or vapourization during high temperature sintering (i.e., above the melting point of Si). The high vacuum pressure (about 10^{-3} Pa) during the SPS coupled with the high vapour pressure of silicon may have led to decomposition of Ti_3SiC_2 thus promoting pore formation via the outward diffusion of Si from the Ti_3SiC_2 grains. This is supported by observation reported elsewhere

[58, 59] and the hypothetical deintercalation reaction leading to pore formation given as follows [60]:



This proposed loss of Si by deintercalation even at sintering temperature below the melting point of silicon ($T_m = 1414^\circ\text{C}$) contributes significantly to the loss of purity in the synthesized sample during the SPS. Investigators have often compensated for the loss of Si during vacuum sintering by silicon over-stoichiometry [47, 61-63] (that is, deviation from 3:1:2 stoichiometric ratio for Ti:Si:C) in the starting mixtures to increase the conversion into Ti_3SiC_2 . Another method involves the systematic addition of a small amount Al in the starting powder mixture [64-66]. The increase in purity with aluminium addition is as follows: as aluminium has a relatively low melting point (660°C), molten Al will promote the diffusion of both Ti and Si atoms thus expediting the formation of Ti_3SiC_2 via solid-liquid reaction at low temperature [67]; molten Al also acts as a deoxidation agent which promotes the synthesis of Ti_3SiC_2 [65]. However, excessive Al may dilute the reactants or react with Ti to form Ti_3Al , thus compromising the phase-purity of Ti_3SiC_2 .

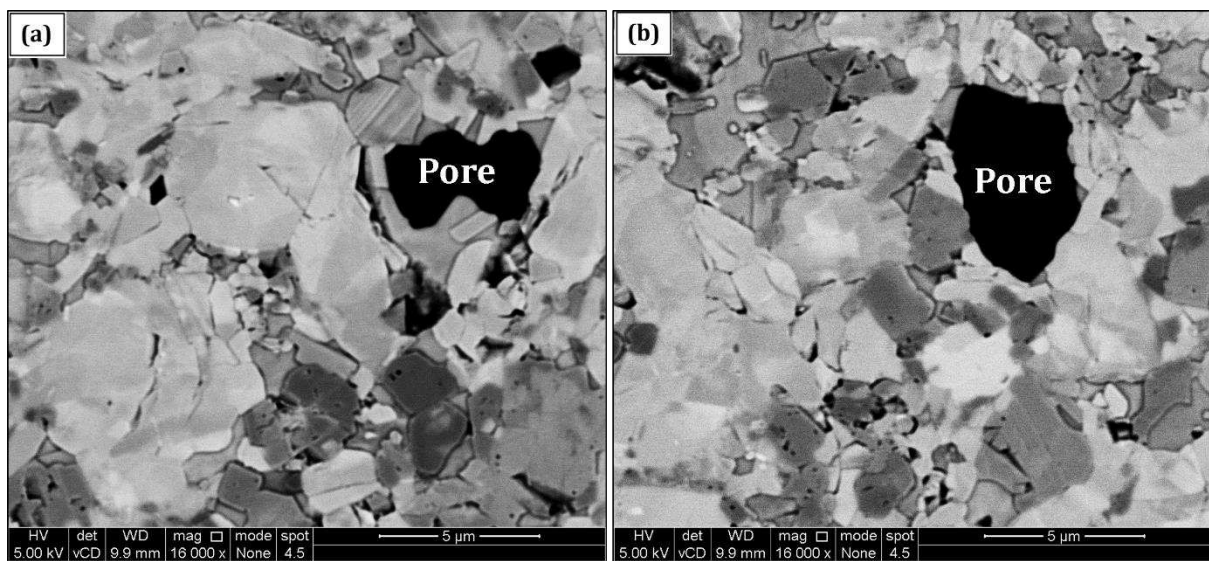


Fig. 13. Pore formation in Ti_3SiC_2 matrix owing to deintercalation of Si under high vacuum pressure.

On the other hand, pore formation may also result from possible carbon uptake from the graphite tooling (graphite paper/die/punch set-up) and its subsequent reaction with Ti_3SiC_2 which will result in bulk compositional shift into a three-phase Ti_3SiC_2 -TiC-TiSi₂ compositional triangle (Fig. 14) following the decomposition reaction thus [68]:

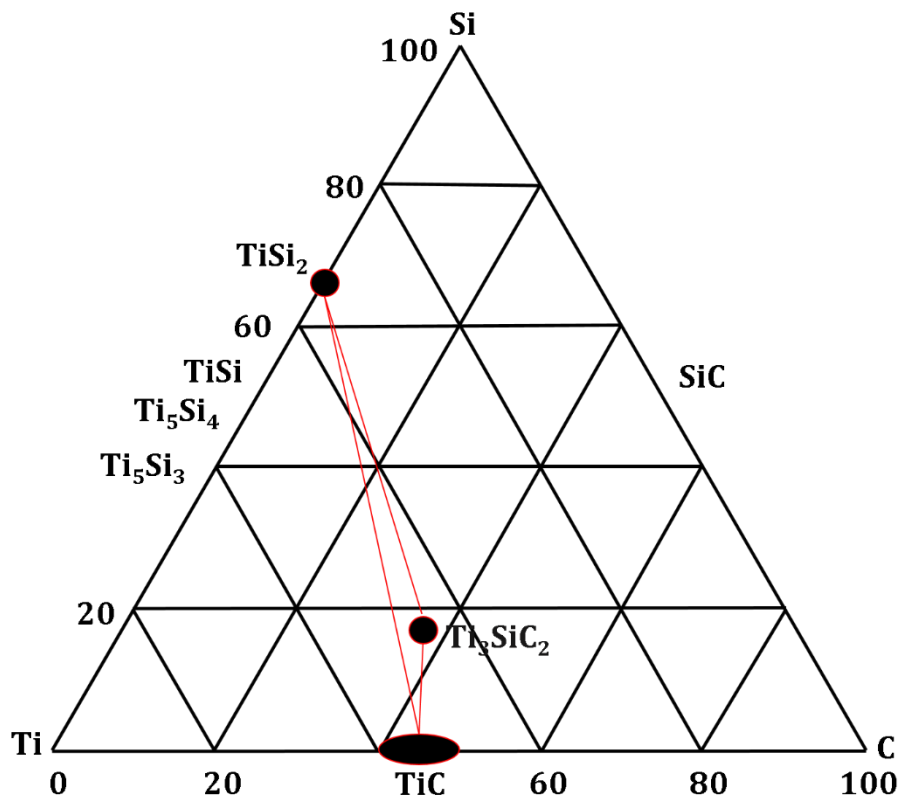
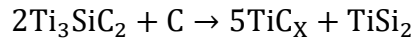


Fig. 14. Compositional diagram in the Ti–Si–C system. The three phases of interest in this work are highlighted using a triangle.

3.6. Vickers-induced deformation microstructure

Vickers microhardness measured from the polished surface of the SPSed disc was ~ 5.8 GPa. This value is somewhat higher as compared to the intrinsic hardness of Ti_3SiC_2 reported to be about 4 GPa [12]. The higher hardness as compared to monolithic phase Ti_3SiC_2 may be associated to the finer microstructure introduced by SPS [61] as well as the presence of TiC

ancillary in the synthesized sample. Optical micrographs (Fig. 15) obtained from the indents showed no sign of lateral cracks emanating from the indentation diagonals as extensive grain pileups around the indents was operative. The ability of Ti_3SiC_2 to contain damage in limited area around the indents is a signature property of the damage tolerance capability reported in MAX phases [12, 13, 69, 70]. Nonetheless, the extent of grain pileup – a microscale deformation mechanism owing to room-temperature plasticity [12] – varied as shown in Fig. 15(a-c) using the same indentation load. According Li et al.[71] asymmetry in the damage zone around indentation is linked to the anisotropic behaviour of Ti_3SiC_2 . This is because favourably oriented grains parallel to the surface will deform by the glide of basal plane dislocations [72] to bring about grain push-outs in the vicinity of the indentation once the compressive stresses are released [12, 71].

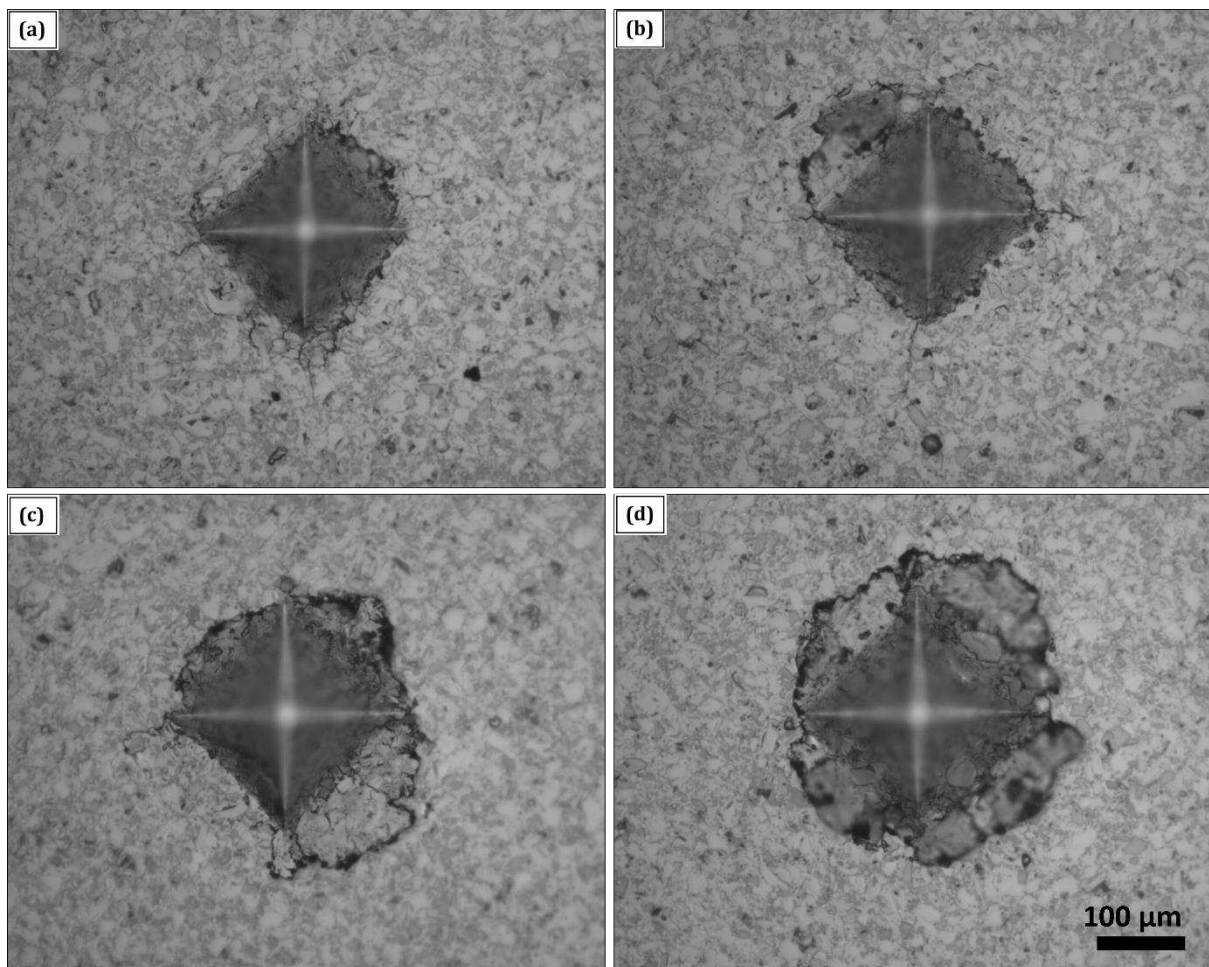


Fig. 15. Optical micrographs showing anisotropic deformation morphology following Vickers indentation.

Fig. 16(a) shows the SEM micrographs obtained from the damage zones around the indentation prints on the bulk sample. No indentation-induced cracks were observed around the indentation diagonals as microdamage appears to be confined in the immediate vicinity of the indents - indicating that Ti_3SiC_2 is damage tolerant. However, the morphology of the grains around the indent further revealed evidence of additional micro-scale deformation mechanisms as shown in Fig. 16(b-d). The energy of an advancing crack appeared to have been consumed due to the plate-like nature of the Ti_3SiC_2 grains leading to diffuse microcracking as shown in Fig. 16(b). In addition to crack deflection, other micro-scale plasticity events occur such as, grain pull-out, delamination (Fig. 16(c)), grain buckling and cavitation (Fig. 16(d)), which renders Ti_3SiC_2 damage tolerant [12, 13]. The observed cavitation after deformation is due to the lack of five independent slip systems needed for polycrystalline ductility in MAX phases [72, 73].

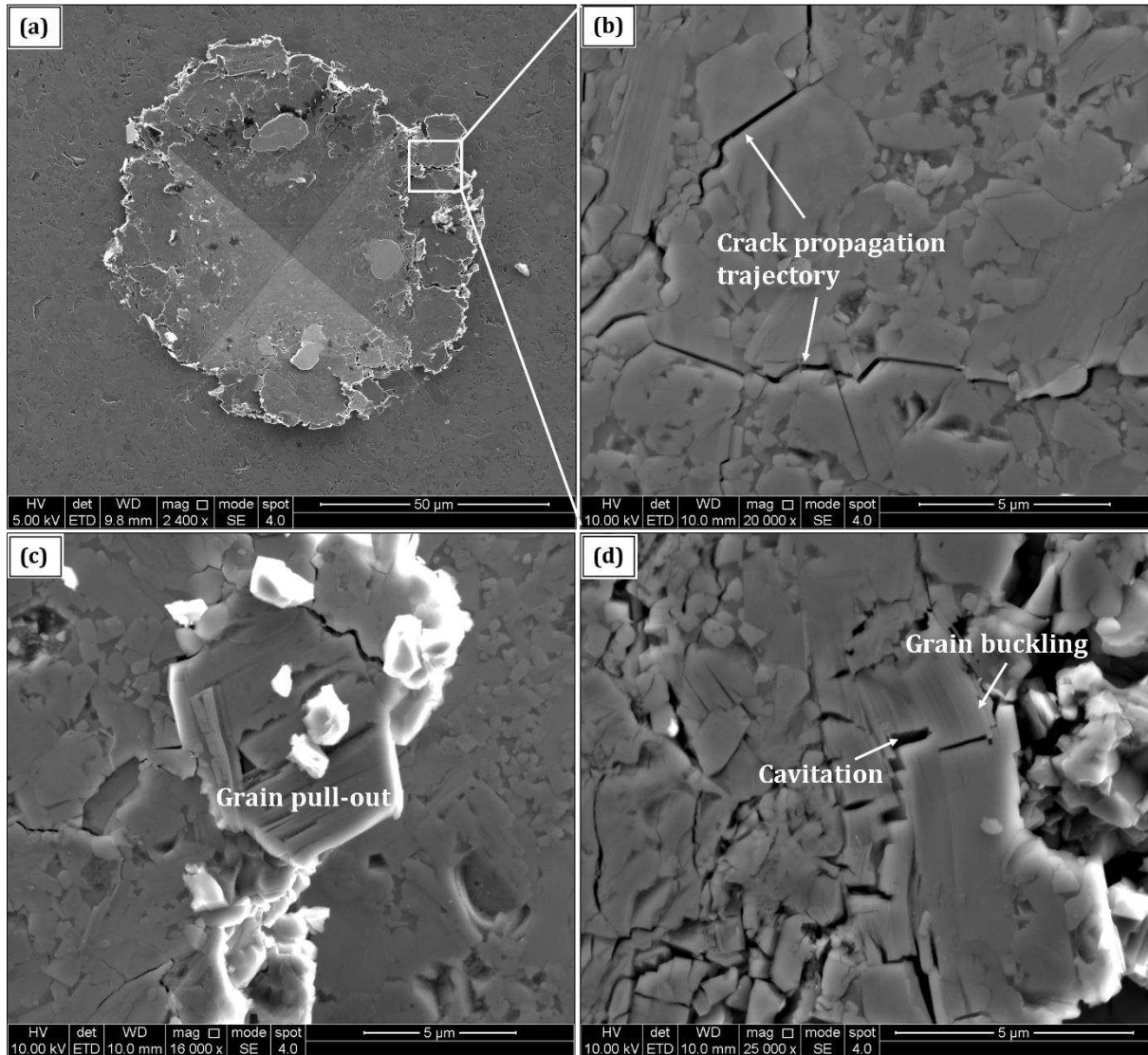


Fig. 16. (a) Scanning electron (SEM) micrographs revealing the morphology around the indent, (b) diffuse microcracking, (c-d) deformation micro-mechanisms in Ti_3SiC_2 .

An intriguing observation during the indentation is the evolution of amorphous-carbon films as shown by EDS elemental map analysis (Fig. 17) and Raman spectroscopy (Fig. 18). The evolution of amorphous carbon layer [74, 75] following indentation scratch, as well as rutile phase of TiO_2 tribofilm [76] further highlights the intrinsic lubricity of Ti_3SiC_2 as reported elsewhere during tribological studies [21] and machining with cutting tools [9].

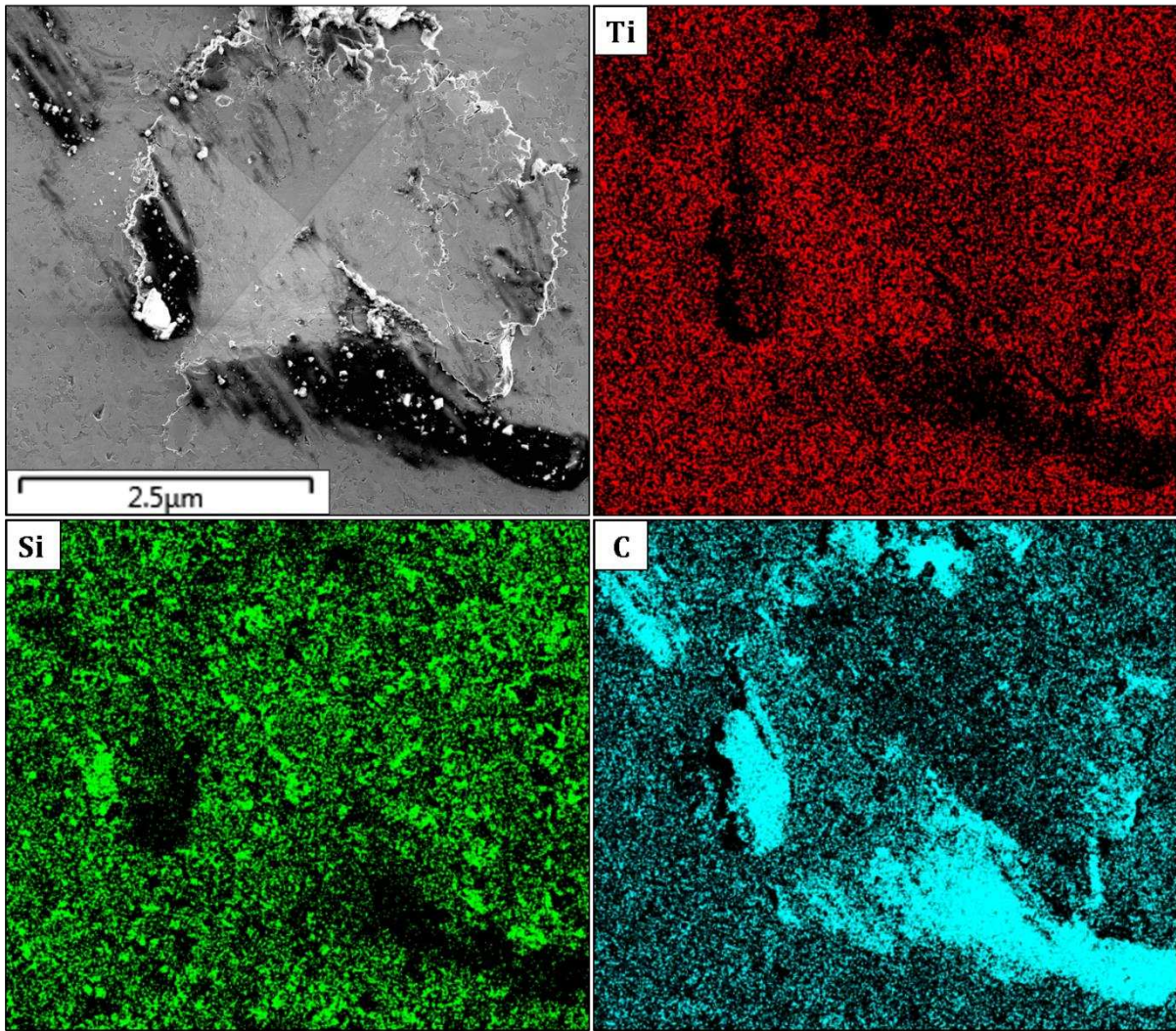


Fig. 17. EDS elemental map of the Vickers indentation print revealing evidence of amorphous carbon around the indent.

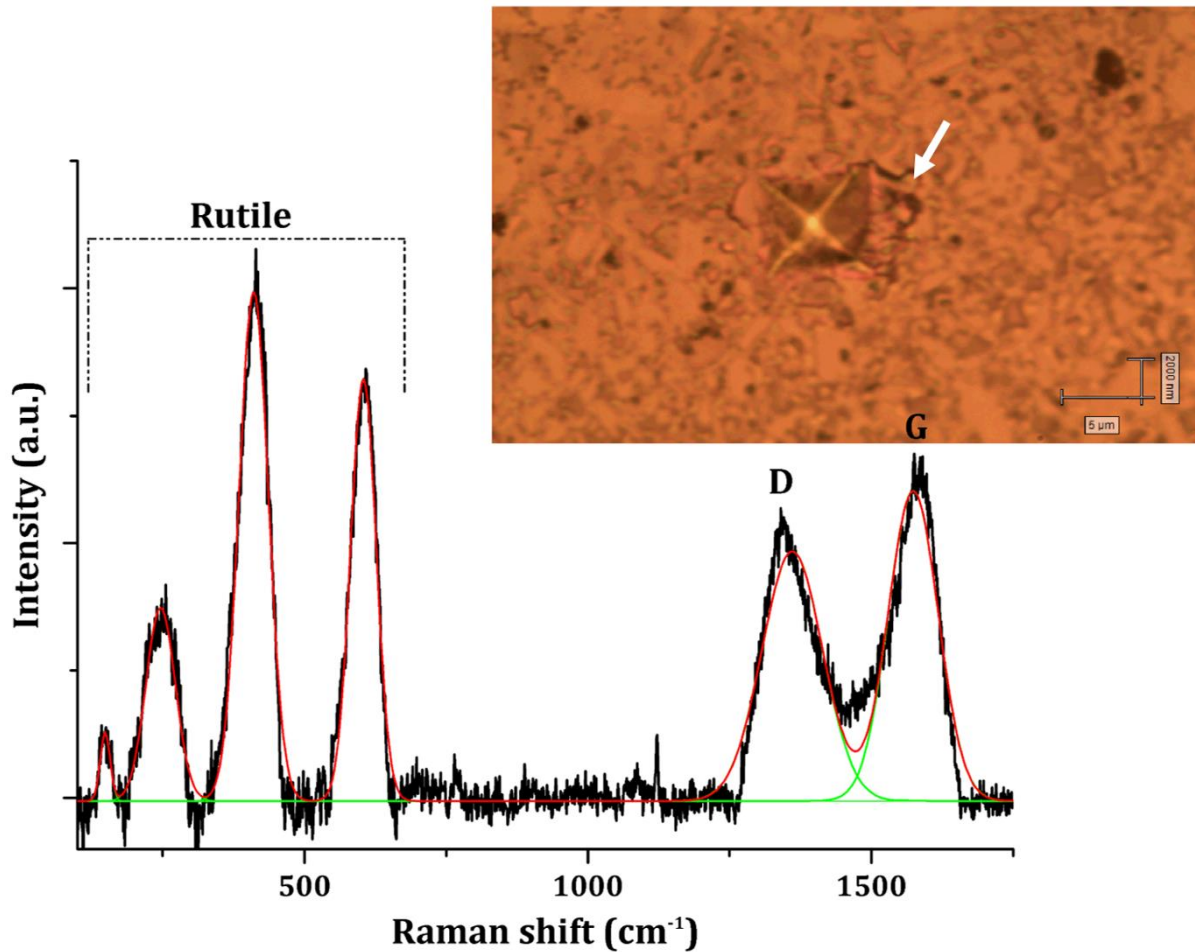


Fig. 18. Raman spectrum collected from the tribofilm region (white arrow) next to the indentation print revealing evidence of tribofilms (rutile (TiO₂) and D & G amorphous carbon Raman vibrational modes).

In order to clarify that the amorphous carbon films are indeed indentation-induced and not as a result of carburization from the graphite tooling employed during the SPS (even though the surface of the bulk sample was polished down to 0.5 μm diamond paste), Raman spectra were collected from the as-synthesized surface (Fig. 19) and polished surface (Fig. 20). For the as-synthesized surface, the Raman spectrum collected from the carburized surface corresponded to vibration mode of crystalline graphite [75]. The D/G intensity ratio (I_D/I_G) used as a graphitization index to monitor the deviation from the crystallinity further differentiates the graphitized layer to the amorphous carbon layer [75]. On the other hand, the Raman spectrum

collected from the polished surface revealed vibrational corresponding to essentially Ti_3SiC_2 [77]. No evidence of non-stoichiometric TiC_x which possesses a Raman active mode which might have formed on the surface due to carburization was detected.

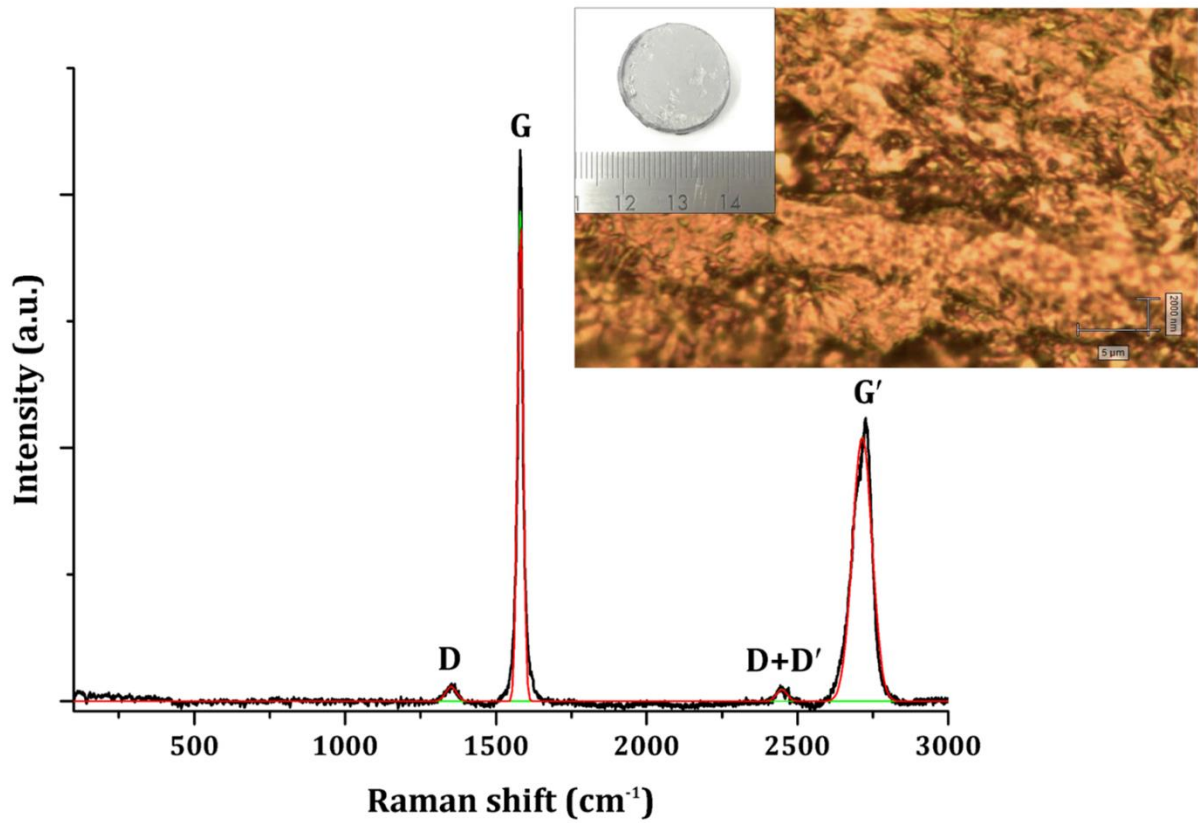


Fig. 19. Raman spectrum collected from the as-synthesized bulk sample surface after SPS. Inset shows the carburized surface where Raman spectrum was collected.

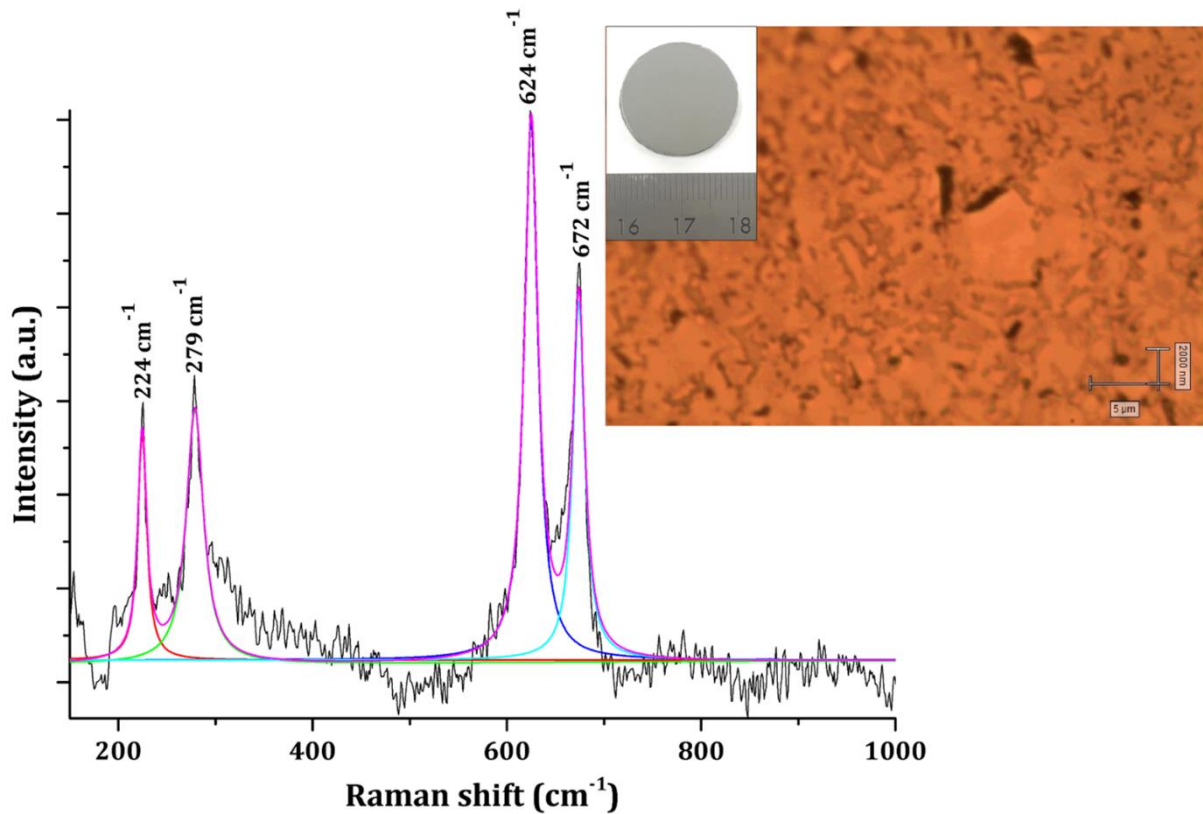


Fig. 20. Raman spectrum collected from the polished surface of the bulk sample. Inset shows the polished surface where the Raman spectrum was collected. Note stoichiometric TiC does not possess Raman active mode.

4. Microstructural and Orientation Relationship

An area from the bulk sample analysed by STEM-EDS is shown in Figs. 21(a-e). The EDS data confirmed the presence of all the three phases i.e. Ti_3SiC_2 , TiC and TiSi_2 . The Ti_3SiC_2 phase typically appear as elongated plate-like grains. The TiC and TiSi_2 phases are essentially defect-free, also, no cracking were observed at the Ti_3SiC_2 -TiC interface due to coefficient of thermal expansion (CTE) mismatch between the two phases as reported elsewhere [78]. The lowest interfacial energy between TiC and Ti_3SiC_2 occurs when (111)TiC is parallel to 001(Ti_3SiC_2), therefore, there is an orientation relationship between TiC and Ti_3SiC_2 in the Ti-Si-C system [79, 80]. Here, we observed similar orientation relationship between TiC and

Ti₃SiC₂ grains. As illustrated in Fig. 21(f), (111)TiC is parallel to (001)Ti₃SiC₂ at the Ti₃SiC₂–TiC interface.

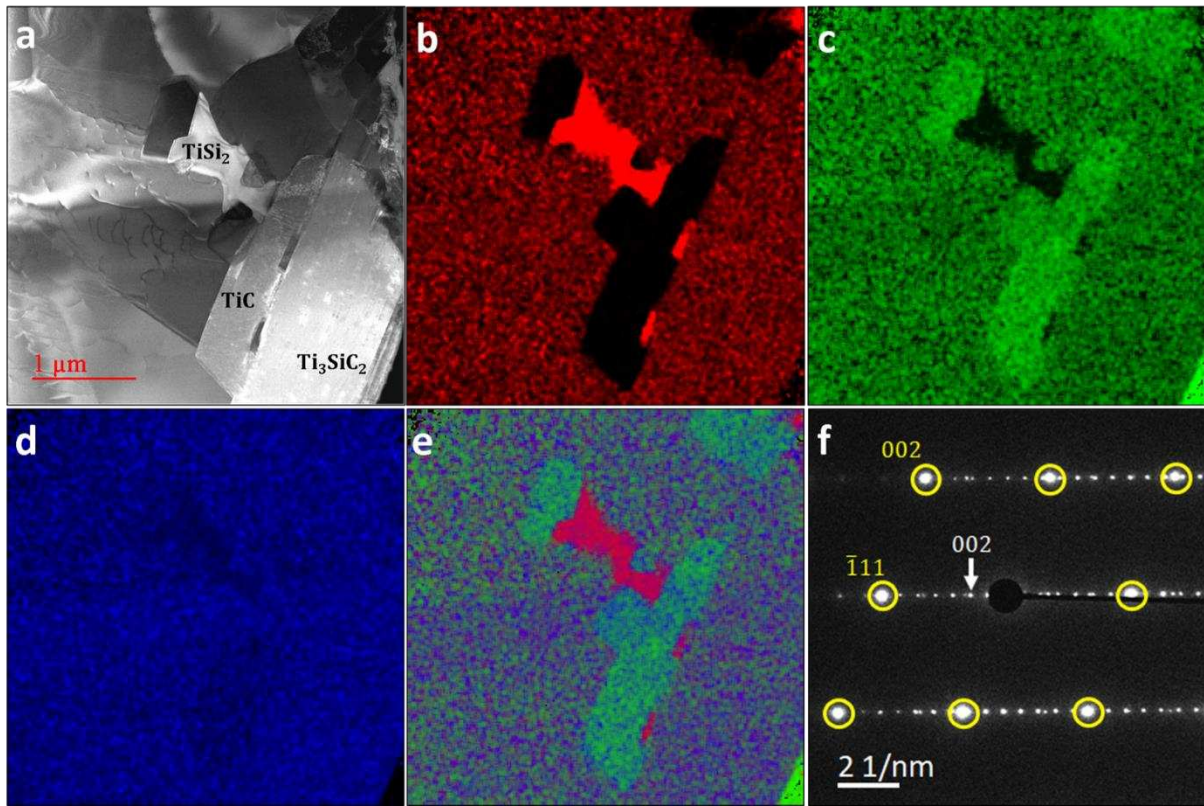


Fig. 21. (a) ADF STEM micrograph obtained from the bulk sample, (b) Si, (c) C and (d) Ti EDS elemental maps from (a). (e) Shows overlay maps of Ti, Si, and C. (f) SAD pattern obtained from the interface of TiC and Ti₃SiC₂ grains where [110]TiC and [100]Ti₃SiC₂ are parallel to the electron beam direction (SAD has been rotated ~ 22° counter-clockwise with regard to (a)). Diffraction spots related to the TiC grain are marked by yellow circles.

5. Conclusions

In this work, Ti₃SiC₂ was successfully fabricated in-situ by powder metallurgy spark plasma sintering using the MAX phase prealloyed starting powder. The reaction mechanism leading to the formation, decomposition and microstructural evolution of Ti₃SiC₂ was discussed, and the main conclusions are as follows:

1. The starting composition, carbon uptake and vacuum pressure during SPS plays a crucial role in high Ti_3SiC_2 conversion.
2. A starting powder mixture with excess silicon and deficient carbon ($3\text{Ti}/(1+x)\text{Si}/(1x)\text{C}$) is needed to compensate for simultaneous Si-loss and carbon uptake, thus leading to high-purity Ti_3SiC_2 .
3. Energy absorbing diffuse microcracking and deformation-induced micromechanisms via basal plane slip renders Ti_3SiC_2 tough and damage tolerant.
4. Ti_3SiC_2 is self-lubricating due to intrinsic rutile and amorphous carbon tribofilm formation.
5. The Maxthal 312 prealloyed starting powder route is suitable in the synthesis of Ti_3SiC_2 if purity of the bulk sample is not of interest such as in the synthesis of MAX phase composites. This is because Si-evaporation will push the overall bulk composition into a two-phase ($\text{Ti}_3\text{SiC}_2\text{-TiC}$) or three-phase ($\text{Ti}_3\text{SiC}_2\text{-TiSi}_2\text{-TiC}$) region with ancillary phases homogeneously distributed in the Ti_3SiC_2 matrix as they formed in-situ and not added as a second phase, thus a reinforcement the MAX phase compound is expected.

References

1. Sokol, M., et al., Big questions in chemistry - on the chemical diversity of the MAX Phases. 2019.
2. Fashandi, H., et al., Synthesis of Ti_3AuC_2 , $\text{Ti}_3\text{Au}_2\text{C}_2$ and Ti_3IrC_2 by noble metal substitution reaction in Ti_3SiC_2 for high-temperature-stable Ohmic contacts to SiC. *Nature Materials*, 2017. 16: p. 814.
3. Fashandi, H., et al., $\text{Ti}_2\text{Au}_2\text{C}$ and $\text{Ti}_3\text{Au}_2\text{C}_2$ formed by solid state reaction of gold with Ti_2AlC and Ti_3AlC_2 . *Chemical Communications*, 2017. 53(69): p. 9554-9557.
4. Naguib, M., et al., Two-Dimensional Nanocrystals Produced by Exfoliation of Ti_3AlC_2 . *Advanced Materials*, 2011. 23(37): p. 4248-4253.
5. Anasori, B., M.R. Lukatskaya, and Y. Gogotsi, 2D metal carbides and nitrides (MXenes) for energy storage. *Nature Reviews Materials*, 2017. 2(2): p. 16098.
6. Naguib, M., et al., Two-Dimensional Transition Metal Carbides. *ACS Nano*, 2012. 6(2): p. 1322-1331.
7. Wang, J., et al., Discovery of hexagonal ternary phase Ti_2InB_2 and its evolution to layered boride TiB. *Nature Communications*, 2019. 10(1): p. 2284.

8. Dahlqvist, M., B. Alling, and J. Rosén, Stability Trends of MAX Phases from First Principles. *Physical Review B*, 2010. 81: p. 220102.
9. Barsoum, M.W. and T. El-Raghy, The MAX Phases: Unique New Carbide and Nitride Materials: Ternary ceramics turn out to be surprisingly soft and machinable, yet also heat-tolerant, strong and lightweight. *American Scientist*, 2001. 89(4): p. 334-343.
10. Barsoum, M.W., MAX phases : properties of machinable ternary carbides and nitrides. 2013: Weinheim, Germany : Wiley-VCH Verlag GmbH & Co. KGaA, 2013.
11. Hwang, S., et al., Machinability of Ti₃SiC₂ with layered structure synthesized by hot pressing mixture of TiC_x and Si powder. *Journal of the European Ceramic Society*, 2012. 32(12): p. 3493-3500.
12. El-Raghy, T., et al., Damage mechanisms around hardness indentations in Ti₃SiC₂. *Journal of the American Ceramic Society*, 1997. 80(2): p. 513-516.
13. Kooi, B.J., et al., Ti₃SiC₂: A damage tolerant ceramic studied with nano-indentations and transmission electron microscopy. *Acta Materialia*, 2003. 51(10): p. 2859-2872.
14. Low, I.M., Vickers contact damage of micro-layered Ti₃SiC₂. *Journal of the European Ceramic Society*, 1998. 18(6): p. 709-713.
15. Tallman, D.J., et al., Effect of neutron irradiation on select MAX phases. *Acta Materialia*, 2015. 85: p. 132-143.
16. Huang, Q., et al., Irradiation resistance of MAX phases Ti₃SiC₂ and Ti₃AlC₂: Characterization and comparison. *Journal of Nuclear Materials*, 2015. 465: p. 640-647.
17. Wang, C., et al., Irradiation-induced structural transitions in Ti₂AlC. *Acta Materialia*, 2015. 98: p. 197-205.
18. Xiao, J., et al., Investigations on Radiation Tolerance of Mn+1AX_n Phases: Study of Ti₃SiC₂, Ti₃AlC₂, Cr₂AlC, Cr₂GeC, Ti₂AlC, and Ti₂AlN. *Journal of the American Ceramic Society*, 2015. 98(4): p. 1323-1331.
19. Lapauw, T., et al., Interaction of Mn+1AX_n phases with oxygen-poor, static and fast-flowing liquid lead-bismuth eutectic. *Journal of Nuclear Materials*, 2019. 520: p. 258-272.
20. Lambrinou, K., Lapauw, T, Jianu, A, Weisenburger, A, Ejenstam, J, Szakálos, P, Vleugels, J., Corrosion-resistant ternary carbides for use in heavy liquid metal coolants. . *Ceramic Engineering and Science Proceedings*, 2016. 36(7): p. 19-34.
21. Magnus, C., J. Sharp, and W.M. Rainforth, The Lubricating Properties of Spark Plasma Sintered (SPS) Ti₃SiC₂ MAX Phase Compound and Composite. *Tribology Transactions*, 2019: p. 1-14.
22. Gupta, S. and M.W. Barsoum, On the tribology of the MAX phases and their composites during dry sliding: A review. *Wear*, 2011. 271(9–10): p. 1878-1894.
23. Magnus, C., et al., Microstructural evolution and wear mechanism of Ti₃AlC₂ – Ti₂AlC dual MAX phase composite consolidated by spark plasma sintering (SPS). *Wear*, 2019. 438-439: p. 203013.
24. Magnus, C. and W.M. Rainforth, Spark plasma sintering (SPS) synthesis and tribological behaviour of MAX phase composite of the family Ti_n+1SiC_n (n = 2). *Wear*, 2019. 438-439: p. 203062.
25. Crisan, A. and O. Crisan, Low-temperature formation of 312 phase in Ti-Si-C ternary compound. *Digest Journal of Nanomaterials and Biostructures*, 2018. 13: p. 155-162.
26. Córdoba, J.M., et al., Synthesis of Ti₃SiC₂ Powders: Reaction Mechanism. *Journal of the American Ceramic Society*, 2007. 90(3): p. 825-830.
27. Sun, Z.M., Progress in research and development on MAX phases: a family of layered ternary compounds. *International Materials Reviews*, 2011. 56(3): p. 143-166.
28. I. M. Low, W.K.P., Thermal Stability of MAX Phases. *Key Engineering Materials*, 2014. 617: p. 153-158.
29. Low, I.-M., An Overview of Parameters Controlling the Decomposition and Degradation of Ti-Based M(n+1)AX(n) Phases. *Materials (Basel, Switzerland)*, 2019. 12(3): p. 473.
30. Munagala, S.P., MAX Phases: New Class of Carbides and Nitrides for Aerospace Structural Applications, in *Aerospace Materials and Material Technologies : Volume 1: Aerospace Materials*, N.E. Prasad and R.J.H. Wanhill, Editors. 2017, Springer Singapore: Singapore. p. 455-465.

31. Zhang, J., et al., Microstructure and Properties of Ti₃SiC₂/SiC Nanocomposites Fabricated by Spark Plasma Sintering. *Composites Science and Technology*, 2008. 68: p. 499-505.
32. Zhang, J., et al., Effect of TiC content on the microstructure and properties of Ti₃SiC₂-TiC composites in situ fabricated by spark plasma sintering. *Materials Science and Engineering: A*, 2008. 487(1-2): p. 137-143.
33. Tzenov, N.V. and M.W. Barsoum, Synthesis and Characterization of Ti₃AlC₂. *Journal of the American Ceramic Society*, 2000. 83(4): p. 825-832.
34. Tang, K., et al., An X-ray diffraction study of the texture of Ti₃SiC₂ fabricated by hot pressing. *Journal of The European Ceramic Society*, 2001. 21: p. 617-620.
35. Barsoum, M.W. and T. El-Raghy, Synthesis and Characterization of a Remarkable Ceramic: Ti₃SiC₂. *Journal of the American Ceramic Society*, 1996. 79(7): p. 1953-1956.
36. Zhang, J., et al., Fabrication of high purity Ti₃SiC₂ from Ti/Si/C with the aids of Al by spark plasma sintering. *Journal of Alloys and Compounds*, 2007. 437(1-2): p. 203-207.
37. Zhou, W.B., B.C. Mei, and J.Q. Zhu, Fabrication of high-purity ternary carbide Ti₃SiC₂ by spark plasma sintering technique. *Materials Letters*, 2005. 59(12): p. 1547-1551.
38. Lapauw, T., et al., A new method to texture dense Mn+1AX_n ceramics by spark plasma deformation. *Scripta Materialia*, 2016. 111(Supplement C): p. 98-101.
39. Ghosh, N.C., Synthesis and Tribological Characterization of In-situ Spark Plasma Sintered Ti₃SiC₂ and Ti₃SiC₂-tic Composites, S.P. Harimkar, K. Kalkan, and R. Singh, Editors. 2012.
40. El Saeed, M.A., F.A. Deorsola, and R.M. Rashad, Optimization of the Ti₃SiC₂ MAX phase synthesis. *International Journal of Refractory Metals and Hard Materials*, 2012. 35: p. 127-131.
41. Gauthier, V., et al., Self-Propagating High-Temperature Synthesis of Ti₃SiC₂: Study of the Reaction Mechanisms by Time-Resolved X-Ray Diffraction and Infrared Thermography. *Journal of the American Ceramic Society*, 2006. 89: p. 2899-2907.
42. Meng, F., B. Liang, and M. Wang, Investigation of formation mechanism of Ti₃SiC₂ by self-propagating high-temperature synthesis. *International Journal of Refractory Metals and Hard Materials*, 2013. 41: p. 152-161.
43. Khoptiar, Y. and I. Gotman, Synthesis of dense Ti₃SiC₂-based ceramics by thermal explosion under pressure. *Journal of the European Ceramic Society*, 2003. 23(1): p. 47-53.
44. Pang, W.K., et al., 15 - Phase and thermal stability in Ti₃SiC₂ and Ti₃SiC₂/TiC/TiSi₂ systems, in *Advances in Science and Technology of Mn+1ax_n Phases*. 2012, Woodhead Publishing. p. 389-413.
45. Zhang, Z.F., et al., Application of pulse discharge sintering (PDS) technique to rapid synthesis of Ti₃SiC₂ from Ti/Si/C powders. *Journal of the European Ceramic Society*, 2002. 22(16): p. 2957-2961.
46. Xu, B., et al., Synthesis of single-phase Ti₃SiC₂ from coarse elemental powders and the effects of excess Al. *Ceramics International*, 2019. 45(1): p. 948-953.
47. Foratirad, H., H. Baharvandi, and M.G. Maraghe, Effect of excess silicon content on the formation of nano-layered Ti₃SiC₂ ceramic via infiltration of TiC preforms. *Journal of the European Ceramic Society*, 2017. 37(2): p. 451-457.
48. Qin, C., et al., Microstructure Characterization and Mechanical Properties of TiSi₂-SiC-Ti₃SiC₂ Composites Prepared by Spark Plasma Sintering. Vol. 47. 2006. 845-848.
49. Kero, I., R. Tegman, and M.-L. Antti, Phase reactions associated with the formation of Ti₃SiC₂ from TiC/Si powders. *Ceramics International*, 2011. 37(7): p. 2615-2619.
50. Wang, X. and Y. Zhou, Solid-Liquid Reaction Synthesis and Simultaneous Densification of Polycrystalline Ti₂AlC. *Zeitschrift fuer Metallkunde/Materials Research and Advanced Techniques*, 2002. 93: p. 66-71.
51. Wang, X. and Y. Zhou, Solid-liquid reaction synthesis of layered machinable Ti₃AlC₂ ceramic. *Journal of Materials Chemistry*, 2002. 12(3): p. 455-460.
52. Guittou, A., et al., Evidence of dislocation cross-slip in MAX phase deformed at high temperature. *Scientific reports*, 2014. 4: p. 6358-6358.
53. Farber, L., et al., Dislocations and Stacking Faults in Ti₃SiC₂. *Journal of the American Ceramic Society*, 2005. 81: p. 1677-1681.

54. Wang, X.H. and Y.C. Zhou, Oxidation behavior of Ti₃AlC₂ powders in flowing air. *Journal of Materials Chemistry*, 2002. 12(9): p. 2781-2785.
55. Sato, F., J. Li, and R. Watanabe, Reaction Synthesis of Ti₃SiC₂ from Mixture of Elemental Powders. Vol. 41. 2000. 605-608.
56. Zhang, Z.-F., et al., A new synthesis reaction of Ti₃SiC₂ from Ti/TiSi₂/TiC powder mixtures through pulse discharge sintering (PDS) technique. *Material Research Innovations*, 2002. 5(3): p. 185-189.
57. Kero, I., M.-L. Antti, and M. Odén, Synthesis of Ti₃SiC₂ by reaction of TiC and Si powders. 2009. p. 21-30.
58. Li, H., et al., Synthesis of Ti₃SiC₂ by pressureless sintering of the elemental powders in vacuum. *Materials Letters*, 2004. 58(11): p. 1741-1744.
59. Li, J.T. and Y. Miyamoto, Fabrication of Monolithic Ti₃SiC₂ Ceramic Through Reactive Sintering of Ti/Si/2TiC. *Journal of Materials Synthesis and Processing*, 1999. 7(2): p. 91-96.
60. Racault, C., F. Langlais, and R. Naslain, Solid-state synthesis and characterization of the ternary phase Ti₃SiC₂. *Journal of Materials Science*, 1994. 29(13): p. 3384-3392.
61. Pourebrahim, A., et al., Low temperature synthesis of high-purity Ti₃SiC₂ via additional Si through spark plasma sintering. *Journal of Alloys and Compounds*, 2019. 789: p. 313-322.
62. Abu, M.J., J.J. Mohamed, and Z.A. Ahmad, Effect of Excess Silicon on the Formation of Ti₃SiC₂ Using Free Ti/Si/C Powders Synthesized via Arc Melting. *ISRN Ceramics*, 2012. 2012: p. 10.
63. Zhang, Z.F., et al., Effects of sintering temperature and Si content on the purity of Ti₃SiC₂ synthesized from Ti/Si/TiC powders. *Journal of Alloys and Compounds*, 2003. 352(1): p. 283-289.
64. Pourebrahim, A., et al., Effect of aluminum addition on the densification behavior and mechanical properties of synthesized high-purity nano-laminated Ti₃SiC₂ through spark plasma sintering. *Journal of Alloys and Compounds*, 2018. 730: p. 408-416.
65. Zou, Y., et al., Effect of Al addition on low-temperature synthesis of Ti₃SiC₂ powder. *Journal of Alloys and Compounds*, 2008. 461(1-2): p. 579-584.
66. Jiaoqun, Z. and M. Bingchu, Effect of Aluminum on Synthesis of Ti₃SiC₂ by Spark Plasma Sintering (SPS) from Elemental Powders. *Journal of Materials Synthesis and Processing*, 2002. 10(6): p. 353-358.
67. Zhu, J.O., et al., Effect of aluminum on the reaction synthesis of ternary carbide Ti₃SiC₂. *Scripta Materialia*, 2003. 49(7): p. 693-697.
68. El-Raghy, T. and M.W. Barsoum, Diffusion kinetics of the carburization and silicidation of Ti₃SiC₂. *Journal of Applied Physics*, 1998. 83(1): p. 112-119.
69. Zhang, Z.F., et al., Micron-scale Deformation and Damage Mechanisms of Ti₃SiC₂ Crystals Induced by Indentation. *Advanced Engineering Materials*, 2004. 6(12): p. 980-983.
70. Murugaiah, A., et al., Spherical Nanoindentations and Kink Bands in Ti₃SiC₂. *Journal of Materials Research*, 2011. 19(4): p. 1139-1148.
71. S. B. Li, J.X.X., L. T. Zhang & L. F. Cheng, Synthesis and some properties of Ti₃SiC₂ by hot pressing of Ti, Si and C powders Part 2 – Mechanical and other properties of Ti₃SiC₂. *Materials Science and Technology*, 2005. 21(9): p. 1054-1058.
72. Barsoum, M. and M. Radovic, Mechanical Properties of the MAX Phases. Vol. 41. 2011. 195-227.
73. Barsoum, M.W., L. Farber, and T. El-Raghy, Dislocations, kink bands, and room-temperature plasticity of Ti₃SiC₂. *Metallurgical and Materials Transactions A*, 1999. 30(7): p. 1727-1738.
74. Tuinstra, F. and J.L. Koenig, Raman Spectrum of Graphite. *The Journal of Chemical Physics*, 1970. 53(3): p. 1126-1130.
75. Santangelo, S., et al., Evaluation of crystalline perfection degree of multi-walled carbon nanotubes: correlations between thermal kinetic analysis and micro-Raman spectroscopy. *Journal of Raman Spectroscopy*, 2011. 42(4): p. 593-602.
76. Challagulla, S., et al., Structure sensitive photocatalytic reduction of nitroarenes over TiO₂. *Scientific Reports*, 2017. 7.
77. Amer, M., et al., The Raman spectrum of Ti₃SiC₂. *Journal of Applied Physics*, 1998. 84(10): p. 5817-5819.

78. Dmitruk, A., et al., Development of Pore-Free Ti-Si-C MAX/Al-Si Composite Materials Manufactured by Squeeze Casting Infiltration. *Journal of Materials Engineering and Performance*, 2019.
79. Tang, K., et al., A study on the orientation relationship between Ti_3SiC_2 and TiC grains. *Materials Letters*, 2002. 57(1): p. 106-109.
80. Lin, Z.J., et al., Microstructural Relationship Between Compounds in the Ti-Si-C System. *Scripta Materialia*, 2006. 55: p. 445-448.